



**EXPERIMENTAL MEASUREMENTS OF STORE SEPARATION USING  
DRY ICE MODELS IN A SUBSONIC FLOW**

THESIS

Michael C. Paul, Second Lieutenant, USAF

AFIT/GAE/ENY/11-M23

**DEPARTMENT OF THE AIR FORCE  
AIR UNIVERSITY**

**AIR FORCE INSTITUTE OF TECHNOLOGY**

**Wright-Patterson Air Force Base, Ohio**

APPROVED FOR PUBLIC RELEASE; DISTRIBUTION UNLIMITED

The views expressed in this thesis are those of the author and do not reflect the official policy or position of the United States Air Force, Department of Defense, or the United States Government. This material is declared a work of the U.S. Government and is not subject to copyright protection in the United States.

AFIT/GAE/ENY/11-M23

**EXPERIMENTAL MEASUREMENTS OF STORE SEPARATION USING  
DRY ICE MODELS IN A SUBSONIC FLOW**

THESIS

Presented to the Faculty

Department of Aeronautics & Astronautics

Graduate School of Engineering and Management

Air Force Institute of Technology

Air University

Air Education and Training Command

In Partial Fulfillment of the Requirements for the  
Degree of Master of Science in Aeronautical Engineering

Michael C. Paul, BS

Second Lieutenant, USAF

March 2011

APPROVED FOR PUBLIC RELEASE; DISTRIBUTION UNLIMITED

**EXPERIMENTAL MEASUREMENTS OF STORE SEPARATION USING  
DRY ICE MODELS IN A SUBSONIC FLOW**

Michael C. Paul, BS

Second Lieutenant, USAF

Approved:

---

Dr Mark F. Reeder (Chairman)

---

date

---

Richard E. Huffman, Lt Col, USAF (Member)

---

date

---

Andrew J. Lofthouse, Maj, USAF (Member)

---

date

## **Abstract**

Despite considerable effort devoted to the study of store separation, the problem remains challenging and important, and the release of a store from a cavity is of particular interest. Testing free-drop store separation from a cavity in wind tunnels proves a difficult task because the models are typically destroyed during the test. Furthermore, there is potential for damage to wind tunnel components or other objects downstream of the test section and its exhaust region. Prior work has shown that small dry ice models released within the test section do not cause damage to the AFIT pressure-vacuum wind tunnel components or vacuum chamber. Rather, the dry ice models typically break apart and sublime harmlessly into gaseous carbon dioxide. Therefore, this study was undertaken to determine whether dry ice models might prove useful in store separation testing. A generic aircraft cavity and release mechanism were constructed for store release in the AFIT low speed wind tunnel. Stores were formed by allowing pressurized liquid carbon dioxide to flow into a mold with a hydrophobic filter at one end and multiple vents for gaseous carbon dioxide to escape, resulting in a solid dry ice model of a store. The store geometry used is a circular cylinder with spherical nosecone, measuring one-inch diameter by 1.8 inches in length. Three small 5mW lasers fitted with pattern generating optics and mounted on the wind tunnel sting illuminated the store and cavity with marker points and reference points, respectively. Three high-speed cameras recorded each test at 700 frames per second and the models were tracked using laser dot projection photogrammetry. In addition, one handheld camera recorded a test for qualitative analysis, and experiments were conducted at nominal freestream velocities of 0, 50, and 100 mph.

## **Acknowledgments**

I would like to express my sincere gratitude to my research advisor, Dr. Mark Reeder, for his guidance throughout this project. In addition, I would like to thank the project sponsors, Rudy Johnson and Jim Grove, from the Aerospace Vehicle Integration and Demonstration Branch of the Air Force Research Labs.

Special thanks to Chris Zickefoose and John Hixenbaugh who spent their time helping me with the wind tunnel and cameras. I am also indebted to the AFIT Model Shop personnel, who spent their time creating the critical components for this thesis.

Michael C. Paul

## Table of Contents

	Page
Abstract .....	iv
Acknowledgments .....	v
Table of Contents .....	vi
List of Figures .....	viii
List of Tables .....	x
Nomenclature .....	xi
Abbreviations .....	xii
I. Introduction.....	1
II. Literature Review .....	4
Three Phases of Separation from a Cavity .....	4
Scaling Laws .....	4
Light Mach Scaling .....	6
Heavy Mach Scaling .....	8
Froude Scaling.....	9
BEGGAR .....	10
Wind Tunnel Testing for CFD Validation.....	11
Free-drop Wind Tunnel Testing .....	12
Captive Trajectory Wind Tunnel Testing .....	14
Dry ice Model Fabrication .....	14
III. Methodology .....	15
Problem Definition .....	15
Scaling Requirements .....	15
Experimental Facilities and Experimental Setup .....	18
Wind Tunnel Equipment .....	19
Wind Tunnel Operations .....	23
Cameras Used for Photogrammetry .....	23
Camera Test Setup.....	25
Laser Grids .....	28
Fabrication of Dry Ice .....	29
Test Procedure .....	32
Image Data Capture.....	34
Limitations.....	37
IV. Results and Analysis.....	39
Raw Imagery .....	39
Single Point Comparison.....	43

PhotoModeler® 3-D Models .....	44
V. Conclusions and Recommendations .....	61
Recommendations for Future Work .....	62
Appendix A: Imagery for Epochs 11-16, $V_{\infty} = 50 \text{ mph}$ .....	64
Appendix B: Repeatability Check .....	68
Bibliography .....	71
Vita .....	73



## List of Figures

Figure 1. Coordinate Notation.....	5
Figure 2. AFIT low-speed wind tunnel .....	19
Figure 3. Wind tunnel ceiling.....	20
Figure 4. Three-view of generic aircraft cavity.....	21
Figure 5. Top-view of release mechanism .....	22
Figure 6. Cavity-view of release mechanism .....	22
Figure 7. The MotionPro X-Stream XS-4 cameras used. This is camera ‘A’ .....	23
Figure 8. The interface on the back of each camera .....	24
Figure 9. The option to designate master camera.....	25
Figure 10. Default camera settings.....	25
Figure 11. Cameras A and C .....	26
Figure 12. Camera B and the computer used to control cameras .....	27
Figure 13. Top-Down view of camera setup .....	27
Figure 14. Side profile of laser setup.....	28
Figure 15. Mold on the fill tube.....	30
Figure 16. Dry ice fabrication setup .....	32
Figure 17. Completed dry ice model .....	33
Figure 18. Example of three images captured .....	35
Figure 19. PhotoModeler® triangulating the expected location of a point .....	36
Figure 20. Three-dimensional model created by PhotoModeler® .....	36
Figure 21. First and last frames processed of each camera at $V_{\infty} = 0 \text{ mph}$ .....	39
Figure 22. First and last frames processed of each camera at $V_{\infty} = 50 \text{ mph}$ .....	40
Figure 23. First and last frames processed of each camera at $V_{\infty} = 100 \text{ mph}$ .....	41
Figure 24. Frames from handheld camera. $V_{\infty} = 100 \text{ mph}$ .....	42
Figure 25. Vertical position of the model for each test. ....	43

Figure 26. Three-view of PhotoModeler® output. Epoch 1, $V_{\infty} = 0 \text{ mph}$ .....	44
Figure 27. Three-view of PhotoModeler® output. Epoch 6, $V_{\infty} = 0 \text{ mph}$ .....	45
Figure 28. Three-view of PhotoModeler® output. Epoch 11, $V_{\infty} = 0 \text{ mph}$ .....	47
Figure 29. Three-view of PhotoModeler® output. Epoch 16, $V_{\infty} = 0 \text{ mph}$ .....	48
Figure 30. Three-view of PhotoModeler® output. Epoch 21, $V_{\infty} = 0 \text{ mph}$ .....	49
Figure 31. Three-view of PhotoModeler® output. Epoch 1, $V_{\infty} = 50 \text{ mph}$ .....	50
Figure 32. Three-view of PhotoModeler® output. Epoch 6, $V_{\infty} = 50 \text{ mph}$ .....	51
Figure 33. Three-view of PhotoModeler® output. Epoch 11, $V_{\infty} = 50 \text{ mph}$ .....	52
Figure 34. Three-view of PhotoModeler® output. Epoch 16, $V_{\infty} = 50 \text{ mph}$ .....	53
Figure 35. Three-view of PhotoModeler® output. Epoch 21, $V_{\infty} = 50 \text{ mph}$ .....	54
Figure 36. Three-view of PhotoModeler® output. Epoch 1, $V_{\infty} = 100 \text{ mph}$ .....	55
Figure 37. Three-view of PhotoModeler® output. Epoch 6, $V_{\infty} = 100 \text{ mph}$ .....	56
Figure 38. Three-view of PhotoModeler® output. Epoch 11, $V_{\infty} = 100 \text{ mph}$ .....	57
Figure 39. Three-view of PhotoModeler® output. Epoch 16, $V_{\infty} = 100 \text{ mph}$ .....	58
Figure 40. Three-view of PhotoModeler® output. Epoch 21, $V_{\infty} = 100 \text{ mph}$ .....	59
Figure 41. Three-view of PhotoModeler® output. Epoch 11, $V_{\infty} = 50 \text{ mph}$ .....	64
Figure 42. Three-view of PhotoModeler® output. Epoch 12, $V_{\infty} = 50 \text{ mph}$ .....	65
Figure 43. Three-view of PhotoModeler® output. Epoch 13, $V_{\infty} = 50 \text{ mph}$ .....	65
Figure 44. Three-view of PhotoModeler® output. Epoch 14, $V_{\infty} = 50 \text{ mph}$ .....	66
Figure 45. Three-view of PhotoModeler® output. Epoch 15, $V_{\infty} = 50 \text{ mph}$ .....	66
Figure 46. Three-view of PhotoModeler® output. Epoch 16, $V_{\infty} = 50 \text{ mph}$ .....	67
Figure 47. Three-view of PhotoModeler® output. Epoch 1, $V_{\infty} = 50 \text{ mph}$ .....	68
Figure 48. Three-view of PhotoModeler® output. Epoch 6, $V_{\infty} = 50 \text{ mph}$ .....	69
Figure 49. Three-view of PhotoModeler® output. Epoch 11, $V_{\infty} = 50 \text{ mph}$ .....	69
Figure 50. Three-view of PhotoModeler® output. Epoch 16, $V_{\infty} = 50 \text{ mph}$ .....	70
Figure 51. Three-view of PhotoModeler® output. Epoch 18, $V_{\infty} = 50 \text{ mph}$ .....	70

## List of Tables

Table 1. Scaling laws compared, $\lambda = 0.05$ .....	16
Table 2. Tests compared against Froude scaling requirements .....	17
Table 3. Comparison of Froude scaling results .....	17
Table 4. Locations for reference point (Point 1022) on the cavity .....	37
Table 5. Location of a marker point (point 1115) for 6 consecutive epochs .....	46

## Nomenclature

AoA	Angle of attack [degrees]
CG	Center of gravity [-]
D	Diameter [inches]
$F_{EJ}$	Ejector force [lb <sub>f</sub> ]
g	Gravitational acceleration constant [ $ft/s^2$ ]
I	Mass moment of inertia [slug ft <sup>2</sup> ]
M	Mach number [-]
m	Mass [slugs]
psia	Pounds per square inch, absolute [ $lb/in^2$ ]
psig	Pounds per square inch, gauge [ $lb/in^2$ ]
$T_{\infty}$	Freestream temperature [R]
t	Time [sec]
$V_{\infty}$	Freestream velocity [ $ft/sec$ ]
$X_{EJ}$	Distance from store CG to location of ejector force [ft]
Z	Vertical location [inches]
$\theta$	Pitch attitude [degrees]
$\lambda$	Model scale factor [-]
$\rho_{\infty}$	Freestream density [ $slugs/ft^3$ ]
$\sigma$	Freestream density ratio [-]
$v$	Freestream velocity ratio [-]

## Superscripts

‘                      Primed quantities refer to scaled dimensions or wind tunnel parameters

## **Abbreviations**

AFIT	Air Force Institute of Technology
AFSEO	Air Force Seek Eagle Office
CFD	Computational Fluid Dynamics
CTS	Captive Trajectory System
HPC	High Performance Computing
IHAAA	Institute for HPC Applications to Air Armament
PMV	PhotoModeler® Video
RP	Rapid Prototype
USAF	United States Air Force

# **EXPERIMENTAL MEASUREMENTS OF STORE SEPARATION USING DRY ICE MODELS IN A SUBSONIC FLOW**

## **I. Introduction**

The United States Air Force (USAF) continues to develop increasingly maneuverable aircraft and weaponry. One way to achieve this goal is to design more neutrally stable platforms that heavily rely on control systems to maintain controlled flight. In addition, current aircraft programs such as the F-22 and F-35 rely on internal weapon storage during certain mission profiles. Despite considerable efforts devoted to the study of store separation, the problem remains challenging and important, and the release of a store from a cavity is of particular interest.

Stores have been carried both internally and externally for years, and each has their own advantages. External storage allows for larger and more numerous stores on a single aircraft. However, the drag and stealth penalties are pushing more stores to internal weapon bays. The USAF uses Computational Fluid Dynamics (CFD) models and wind tunnel testing to certify stores for operational flights. In the wind tunnel, “the typical analysis involves the use of time averaged store aerodynamic loads to estimate the effect of the aircraft flowfield on the store trajectory” [1]. While this usually yields satisfactory results, there have been incidents that justify the use of flight-testing to validate results. However, due to the high cost and time requirements for flight-testing, only a limited number of conditions are flight-tested. Moving stores to internal bays make testing and prediction increasingly difficult because “the store must fly in the weapons bay and shear layer before it even gets to the aircraft flowfield” [1]. Both locations are unsteady environments in which the store was not designed to operate. As Johnson, Stanek and Grove state, “The combined trends toward internal carriage of weapons in modern aircraft and the design of new weapons to be neutrally stable for increased performance have increased the probability that unsteady aerodynamics will affect store separation trajectories” [1]. Most current

techniques applied in practice do not account for unsteady flow computationally or in wind tunnel tests [1].

Previous wind tunnel experimental work falls in two main categories: (1) captive store testing where the store is placed on a sting to measure forces and moments as the store is traversed from the cavity in a controlled manner, or (2) free drop testing where the store is dropped from the cavity and tracked through the test section of the wind tunnel. As noted by Johnson et al, the first category,

“Places the store to be separated on a sting or strake that allows positioning of the store in the aircraft flow field. [It] is capable of generating both quasi-time accurate trajectories and a ‘grid’ of store aerodynamic coefficients. Mechanical limitations prevent fully time accurate trajectory modeling with [captive trajectory system] (CTS) testing” [1].

The second category allows for more realistic modeling because the store responds naturally, but scaling issues often skew the results. Many tests use light Mach scaling because of the model densities or stagnation pressures needed for accurate results. However, allowing a store to pass freely from the test section downstream poses a great risk to wind tunnel hardware. Partly for this reason, Murray et al. [2] used a relatively soft SLA plastic JDAM model to minimize downstream damage. “Wind tunnel testing of small-scale stores has been used to model the separation event, but is not typically used for production weapons because of the approximations used in scaling which make accurately determining trajectories of the full-scale store difficult” [1].

Prior work has shown that small dry ice models accidentally released as part of an ongoing ablation rate study do not cause damage to the Air Force Institute of Technology (AFIT) pressure-vacuum wind tunnel components or vacuum chamber. Rather, the dry ice models break apart and sublime harmlessly into gaseous carbon dioxide. Therefore, this study was undertaken to determine whether dry ice models might prove useful in free-drop store separation testing. A generic aircraft cavity, release mechanism, and dry ice stores were constructed for

testing in the AFIT low speed wind tunnel to verify procedures of making and tracking the models.

The overarching goal of the project was to verify dry ice models could be applied in free-drop testing in a high Mach number pressure-vacuum wind tunnel. As a subset of that goal, the research objective of this thesis was to utilize non-intrusive measurement techniques to track store separation in a low speed wind tunnel using the same photographic equipment. Dry ice store models were released at low Mach numbers from a generic aircraft cavity. Three high-speed cameras recorded laser dots projected on the model surface. Dot projection photogrammetry tracked the model location in three dimensions as the store fell through the cavity into the tunnel freestream.



## **II. Literature Review**

### **Three Phases of Separation from a Cavity**

A store separation from an internal cavity has three distinct phases. The first phase is when the store is inside the cavity. This environment has high acoustic loads and unsteady vortex shedding from the leading edge of the cavity. The second phase is when the store crosses the shear layer. This phase is highly unsteady and different areas of the store experience different flow fields based on vertical position. The last phase is when the store is completely outside of the cavity [3]. This phase is comparatively steady and the closest to freestream conditions. “While slender body theory and asymptotic methods are applied in phases 1 and 3, the shear layer is modeled as a steady inviscid vortex sheet. This is rationalized by observing that the unsteady motions of the shear layer are three orders of the magnitude faster than the time scale of the separating body” [1]. Shalaev, et al, showed that the pitch behavior in phase 3 strongly depends on the initial conditions [3]. Once the store is beyond the aircraft flowfield it is considered “separated” and internal guidance and control take over. Whether using a passive or active control system, stores are designed to fly in steady flowfields, meaning unsteady flowfields may have dramatic effects. The store separation proves a critical and challenging phase of flight to model.

Traditional store separation modeling focuses on the initial half second of flight. In a clean separation, the store will travel up to 15 feet in this time and is unlikely to impact the aircraft. “During this short time period the aerodynamics of the weapon being released are modified by the influence of the aircraft aerodynamics which can significantly modify the expected store performance” [1].

### **Scaling Laws**

Wind tunnel testing is used extensively because store separation flight-testing is extremely time consuming, expensive and potentially risky. To reproduce basic aerodynamic

characteristics both aircraft and store models are linearly scaled down to suit wind tunnel dimensions using geometric similarity. The mass properties of the store model must be taken into consideration to provide representative tests. The three basic scaling methods are light Mach scaling, heavy Mach scaling, and Froude scaling, each discussed below. Both light and heavy Mach scaling maintain Mach number and therefore allow for compressible flow effects to be taken into account while Froude scaling is often satisfactory for modeling flight Mach numbers less than 0.6 [4].

When discussing the scaling relationships, it is important to understand the coordinates these transformations use. As shown in Figure 1, the wind axis is defined as such: positive x is measured parallel and opposite the direction of flow. Positive y is measured perpendicular to the flow; for aircraft models, positive y is down the right wing. Positive z is measured down, perpendicular to the earth's surface. The heading angle, theta, is the angle above the earth horizontal.

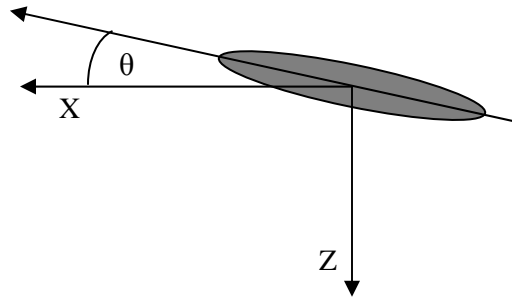


**Figure 1. Coordinate Notation**

For the linear scaling discussed below, the three main scaling factors are the model scale factor, the density ratio and the freestream velocity ratio, as below.

$$\lambda = \text{model scale factor}$$

$$\sigma = \rho'_{\infty} / \rho_{\infty} \tag{1}$$

$$v = V'_{\infty} / V_{\infty}$$

The prime terms denote the wind tunnel values. This analysis assumed a 5% scale factor. Because this research aimed to model a M=0.8, 10,000 ft. release in a low speed wind tunnel at 500 ft. MSL, both the density and velocity ratios were less than one.

### ***Light Mach Scaling***

Light Mach scaling tests match the flight Mach number by allowing other variables to change [4]. Light scaling typically uses low-density models moving through a high-density fluid. This matches angular motion well, but the higher dynamic pressure prevents accurate vertical displacement of the store model. Ejecting the model often induces an increased downward acceleration and pushes the model through the shear layer. The user needs to know the ejection force and velocity to achieve an accurately scaled parameter. Light scaling is simpler to achieve, but requires more complicated release mechanisms and post run data processing to correct for inaccuracies.

Light Mach scaling matches angular motion response by arbitrarily increasing the desired gravitational constant in the scaled experiment. Using the velocity scaling from Froude scaling and setting the desired gravitational constant to

$$g' = g (v^2)/(\lambda) \quad (2)$$

the scaling relationships are as follows:

$$\begin{aligned}
Z' &= Z(\lambda) \\
\Theta' &= \Theta \\
m' &= m(\sigma)(\lambda^3) \\
I' &= I(\sigma)(\lambda^5) \\
F'_{EJ} &= F_{EJ}(\sigma)(v^2)(\lambda^2) \\
X'_{EJ} &= X_{EJ}(\lambda) \\
V'_\infty &= V_\infty \sqrt{(T'_\infty/T_\infty)} \\
t' &= t(\lambda/v)
\end{aligned} \tag{3}$$

The length scale,  $Z$ , scales by the model scale factor while the store attitude,  $\Theta$ , does not require scaling. Because the equations of motion are dependent on the weapon mass and moments of inertia, they must be accurately scaled to reproduce the full-scale weapon motion. Light scaling relies on an ejector motor to penetrate the high-density flow. The ejector force and location are scaled based on tunnel capabilities and model scale factor. The required tunnel velocity is a function of the full-scale freestream velocity and the temperature ratio. The time scale is a function of the scale factor and the velocity ratio.

As Johnson, Stanek, and Grove noted [1], “It is well known that the light scaling laws used to develop the store model increases the sensitivity of the store trajectory to the aerodynamic loads over that which would be seen at full scale”. As a result, the deviations are the ‘worst case scenario’ due to magnified aerodynamic loads relative to the other forces.

The work of Murray et al. [2] used light scaling to model separation dynamics of a GBU-38 JDAM. They experienced difficulties in matching the scaled model weight due to manufacturing constraints. In an effort to match store dynamics, a complicated release mechanism used a pneumatic solenoid release pin and two pressurized ejector pins to provide down force. The variables considered include peak ejection force, end-of-stroke velocity, stroke

length, variable pitch control, and ejector location. The dry ice model and wind tunnel capabilities allows for the much simpler release mechanism described in Chapter 3.

### ***Heavy Mach Scaling***

Heavy Mach scaling tests use high density models moving through a low density fluid. Wind tunnel dynamic pressure must be much lower than the flight value requiring high model density, although mass distribution remains the same. The angular motion suffers in accuracy compared to light scaling. For example, the reduced dynamic pressure decreases pitch damping, causing pitch oscillations much greater than those of the full-scale store [4]. The difficulty with heavy Mach scaling lies in the very high mass densities or very low stagnation pressures required during testing. However, assuming the gravitational constant is equal to that of the full scale test makes the experimental setup simpler because it removes the requirement for an ejector motor.

In this technique, the Mach number for the scaled test is set equal to that of the wind tunnel test [4], which results in approximately the same velocities. The resulting scaling relationships are as follows:

$$\begin{aligned}
 Z' &= Z(\lambda) \\
 \Theta' &= \Theta \\
 m' &= m(\sigma)(v^2)(\lambda^2)(g/g') \\
 I' &= I(\sigma)(v^2)(\lambda^4)(g/g') \\
 F'_{EJ} &= F_{EJ}(\sigma)(v^2)(\lambda^2) \\
 X'_{EJ} &= X_{EJ}(\lambda) \\
 V_{\infty}' &= V_{\infty}\sqrt{(T_{\infty}'/T_{\infty})} \\
 t' &= t\sqrt{\lambda(g/g')}
 \end{aligned} \tag{4}$$

Compared to light Mach scaling, many of the relationships are the same. These relationships state the model density must be much higher than that of the store unless the wind tunnel dynamic

pressure can be significantly reduced [4]. Mass and mass moment of inertia lose an order of  $\lambda$  for the gravitational constant ratio. In addition, the time scale replaces the velocity ratio with the gravitational constant ratio. Without arbitrarily increasing the gravitational constant as in light Mach scaling, the relationships become:

$$\begin{aligned} m' &= m(\sigma)(v^2)(\lambda^2) \\ I' &= I(\sigma)(v^2)(\lambda^4) \\ t' &= t\sqrt{\lambda} \end{aligned} \tag{5}$$

These relationships were used in the analysis below.

### ***Froude Scaling***

Froude scaling tests use many of the same scaling relationships. The Froude number, which relates buoyancy forces to inertial forces, acts as the velocity scaling law. Because of this, Froude scaling does not match Mach number, or accurately model the resulting compressibility effects. However, it reproduces the motion of the store when the Mach number at full-scale flight conditions is within a range where compressibility is not a factor.

Froude scaling is the most difficult to reproduce to because of the extreme model densities or stagnation pressures needed to accurately scale the store. The velocity scaling ratio is the Froude number and the gravitational constant is not generally considered a variable. The relationships are below:

$$\begin{aligned}
Z' &= Z(\lambda) \\
\Theta' &= \Theta \\
m' &= m(\sigma)(v^2)(\lambda^2)(g/g') \\
I' &= I(\sigma)(v^2)(\lambda^4)(g/g') \\
F'_{EJ} &= F_{EJ}(\sigma)(v^2)(\lambda^2) \\
X'_{EJ} &= X_{EJ}(\lambda) \\
V'_\infty &= V_\infty \sqrt{(\lambda)(g'/g)} \\
t' &= t(\lambda/v)
\end{aligned} \tag{6}$$

Again, without arbitrarily increasing the gravitational constant as in light Mach scaling, the relationships become:

$$\begin{aligned}
m' &= m(\sigma)(v^2)(\lambda^2) \\
I' &= I(\sigma)(v^2)(\lambda^4) \\
V'_\infty &= V_\infty \sqrt{(\lambda)}
\end{aligned} \tag{7}$$

These relationships appear the same as heavy Mach scaling, except for the velocity and time scales. The difference comes when accounting for the velocity change [4]. The difference in wind tunnel velocity propagate through the velocity ratio,  $v$ , and all other relations. The time scale matches that of light Mach scaling. Froude scaling does not match Mach number, which is a big concern for supersonic testing, when shockwaves play an integral role in store motion.

## BEGGAR

The BEGGAR code is a CFD code utilized by the Air Force to compute carriage loads and store separation trajectories. It originated in the Wright Laboratories before transferring to Air Force Seek Eagle Office (AFSEO) at Eglin Air Force Base in 1993, where its development continued [5]. Freeman and Jolly [6] detail AFSEO successes using BEGGAR.

BEGGAR completes four operations at each time step to determine the body's motion: (1) assembles the grids, (2) solves the flow governing equations, (3) integrates the pressure and viscous stresses along the body to determine forces and moments acting on the body, (4) solves the equations of motion to determine the new body location and orientation [5]. BEGGAR automates grid assembly with user inputs of the grids, the required transformations to orient the grids properly, and the identification of boundaries and planes of symmetry. According to Rizk, Ellison and Prewitt [5], "BEGGAR's flow solver provides time-accurate inviscid and viscous flow field solutions based on a finite-volume cell-centered discretization. Turbulence modeling is introduced through the use of the Baldwin-Lomax algebraic model or the  $k - \epsilon$  two-equation model with wall functions" [5]. BEGGAR integrates the solution to the flow equations to calculate forces and moments, which are inputs into the 6DOF (Six Degrees of Freedom) solver, which solves the equations of motion. AFSEO upgraded BEGGAR's original 6DOF solver to analyze moving components, such as fins that deploy after store release [5].

This brief overview of BEGGAR highlights the complexity of the code and its ability to accurately model store separation. However, as Cenko et al. discussed, CFD codes are only useful when validated with accurate wind tunnel data. The technique discussed in this paper accurately tracks and measures store location and orientation after release.

### **Wind Tunnel Testing for CFD Validation**

The need to meet wartime requests rapidly at minimal developmental risk drove the High Performance Computing (HPC) Modernization Program Office to establish the Institute for HPC Applications to Air Armament (IHAAA). The Air Force, Army, and Navy each have proven CFD modeling and simulation software used to augment flight and wind tunnel testing for weapon development and integration [7]. IHAAA works on projects such as modeling the release of weapons with deployable control surfaces and certifying the LITENING AT pod. IHAAA estimates it saves \$80,000-\$95,000 per flight, with multiple flights needed for each project [7].



However, CFD models require flight test and wind tunnel data for validation. In fact, “the reason that CFD was a practical alternative was that there existed substantial wind tunnel and flight test data for both the F/A-18C/D aircraft and the stores that were tested” [7]. Wind tunnel testing remains an important tool for store separation analyses. In fact, Cenko et al. concluded, “For cases where large amounts of test data are required, the wind tunnel has no match at the present time. Even though these conditions have been met, the need for wind tunnel testing has not been eliminated” [7].

### **Free-drop Wind Tunnel Testing**

Johnson, Stanek and Grove [1] review CFD results for the Small Smart Bomb separating from an F-111 aircraft and a GBU-12 from a B-52 aircraft. Small scale drop testing demonstrates the effect of unsteady flow on store separation. Typical wind tunnel data collects time averaged loads, which cannot detect the trajectory sensitivity to the time of weapon release found in CFD results. Flight testing has not investigated the effects of bay unsteadiness due to the cost and complexity required for repeated tests. However, “carefully designed and conducted small scale drop testing in wind tunnels provides a means to identify the effect of unsteady weapons bay aerodynamics on store separation trajectories” [1]. Tests occurred with a generic store from a cavity with  $L/D = 6.0$  into a Mach 1.45 freestream. Dynamic pressure and balance data were collected from 24.4 Hz to 50 kHz. In addition, 6% scale drop tests occurred with a Mk-82 model from a B-1B model, using light scaling. Tests raised questions about repeatability of the ejection mechanism [1].

Shalaev et al. investigated the motion of slender bodies separating from rectangular cavities into low subsonic freestreams. The first part of their work presents the three phases of separation discussed above in Three Phases of Separation from a Cavity. They continue with a combined asymptotic and numerical approach to “solve aerodynamic problems relevant to separation of a thin body of revolution from rectangular cavities into subsonic or transonic flows”

[3]. Like many previous studies, the unsteady motions of the shear layer are time averaged. The flow over the separating body was modeled using slender body theory. A sixth-order Runge-Kutta scheme numerically integrates the vertical and pitching body motions to calculate the body trajectory in all phases of separation [3]. These results are compared with wind tunnel data.

Tests were performed from a  $L/D = 5.0$  cavity into a  $0.12 < M < 0.23$  freestream. A range of models was tested with 0.75-inch diameter and 11.5-inch to 12-inch length. The main difference arises in model mass, as they range from 8.72 grams to 111.85 grams [3]. The models were released by withdrawing pins at the nose and tail.

Murray et al. used a similar setup in their work “to examine the phase relationship between the store release and the cavity pressure oscillations” [2]. The model was  $1/15^{\text{th}}$  scale GBU-38 designed using light scaling. The resulting model had 18.8 mm diameter, 16 cm length and 49 gram mass. Test drops were performed from a rectangular  $L/D = 6.0$  cavity into a Mach 1.5 freestream [2].

The model was optically tracked, similar to Particle Image Velocimetry (PIV) methods, using a single camera and high-intensity LED strobe light. Frames were captured at 4 kHz [2]. Two black dots on the model surface defined position and attitude through the test. In this research, time constraints forced a reduced frame rate due to tracking of 30-45 points per frame.

Because the model was designed using light scaling, a properly sized ejector had to be created. A release pin suspends the model in the cavity while the ejector pistons captivate the store. When activated, “a pneumatic solenoid activates the release pin giving a near-instantaneous release. The two ejection pistons share a common plenum to provide a common pressure to both pistons” [2]. This system ensured correct ejector force, velocity and stroke for consistent data. Murray et al. built models with an aluminum strongback to distribute loads during ejection. Installing such supports would negate the purpose of using dry ice: to minimize or eliminate wind tunnel damage.

## **Captive Trajectory Wind Tunnel Testing**

Bjorge et al. [8] investigated store-cavity interaction using fast-response pressure transducers, high-speed Schlieren photography, and pressure-sensitive paint (PSP). A store model on a sting was extended into the Mach 1.8 and 2.9 freestream from a cavity with  $L/D = 3.6$ . Supersonic flow past an open cavity causes two significant issues. First, the generated resonance leads to deterioration of the weapon and cavity structure. Second, unsteady aerodynamics can cause unpredictable separations. The trajectory of a store after release needs to be predictable and controllable for operational certification.

## **Dry ice Model Fabrication**

Callaway et al. looked at low temperature ablators in supersonic flows. Their work, “performed at the [AFIT] high speed wind tunnel facility to measure ablation rates on three-dimensional surfaces using dry ice exposed to a Mach 3 free stream” [9] developed the model fabrication and measurement techniques used in this research. Callaway worked to form models by injecting liquid  $\text{CO}_2$  directly into a prescribed mold. The process is based on the work by Kohlman and Richardson, who investigated the use of dry ice wind tunnel models [10]. A full description of the method is included in section Fabrication of Dry Ice.

In addition, Callaway used dot projection photogrammetry to measure ablation rates. This research used a similar setup. For this thesis, the larger wind tunnel dimensions dictated the use of different camera lenses. The PhotoModeler® software reproduced points on the three-dimensional models from the high speed camera imagery.

### **III. Methodology**

#### **Problem Definition**

The overarching goal of the project was to verify dry ice models could be applied in free drop testing in a high Mach number pressure-vacuum wind tunnel. As a subset of that goal, the research objective of this thesis was to utilize non-intrusive measurement techniques to track store separation in a low speed wind tunnel using the same photographic equipment. Dry ice store models were released at low Mach numbers from a generic aircraft cavity. Three high-speed cameras recorded laser dots projected on the model surface. Dot projection photogrammetry tracked the model location in three dimensions.

#### **Scaling Requirements**

The three scaling laws were used to determine the proper model properties and test conditions necessary to model a Mk-81 released from an aircraft at Mach 0.8 at 10,000 ft. The small size of this munition kept the scaling factor reasonable. At a 5% scale, the weapon scaled down to a model with a 0.5-inch diameter and 3.7-inch length. The user calculated the model mass moment of inertia and density using the model dimensions and mass. The mass moment of inertia was not publicly available for the Mk-81. As a result, this parameter was not scaled or used in the initial scaling law comparison. The user calculated the model density using the model dimensions and mass. The mass moment of inertia was not publicly available for the Mk-81. As a result, this parameter was not scaled or used in the initial scaling law comparison. The user calculated the model density using the model dimensions and mass. The mass moment of inertia was not publicly available for the Mk-81. As a result, this parameter was not scaled or used in the initial scaling law comparison.

Table 1 compares the three laws so it can be determined which scaling law best matches the research objectives and equipment capabilities. The user calculated the model density using

the model dimensions and mass. The mass moment of inertia was not publicly available for the Mk-81. As a result, this parameter was not scaled or used in the initial scaling law comparison.

**Table 1. Scaling laws compared,  $\lambda = 0.05$**

	<b>Diameter</b> (in)	<b>Length</b> (in)	<b>Airspeed</b> (mph)	<b><math>\theta</math></b> (deg)	<b>m</b> (lbs)	<b>Dry ice</b> <b>Density</b> (lb <sub>m</sub> /ft <sup>3</sup> )	<b>I</b> (slug ft <sup>2</sup> )	<b>F<sub>EJ</sub></b> (lb <sub>f</sub> )	<b>X<sub>EJ</sub></b> (ft)	<b>t</b> (sec)
<b>Mk-81 [11]</b>	9.0	74.0	618	0	262	-	?	0	0	0.50
<b>Froude Scaling</b>	0.45	3.7	138	0	0.010	65	?	0	0	0.11
<b>Heavy Scaling</b>	0.45	3.7	580	0	0.389	1141	?	0	0	0.02
<b>Light Scaling</b>	0.45	3.7	580	0	0.022	65	?	0	0	0.02

Froude scaling requires a wind tunnel velocity of 138 mph and model density of  $65 \text{ lb}/\text{ft}^3$ .

Previous testing found dry ice model densities of approximately  $65 \text{ lb}/\text{ft}^3$  repeatable [9], making Froude scaling possible if matching flight tests at 10,000 ft. altitude. Scaling the initial 0.5-seconds of primary concern in full scale testing [1] resulted in a time scale of 0.11 seconds.

At Mach 0.8, the full-scale weapon would experience compressibility effects. To match Mach number, heavy Mach scaling and light Mach scaling were also considered. Both required test velocities of 580 mph and time scales of 0.02 seconds. Heavy scaling required a model density of  $1141 \text{ lb}/\text{ft}^3$ . With model density limited to approximately  $65 \text{ lb}/\text{ft}^3$ , heavy scaling was unreasonable to attempt. For light scaling, the model densities required were the same as Froude scaling.

Froude scaling yielded manageable experimental requirements because the necessary model densities have been produced in the past and wind tunnel velocity was less than the 145 mph limit of the wind tunnel. Froude scaling avoided the exaggerated angular motions of light scaling, but at the cost of modeling compressibility effects.

After examining the available resources, the scaling laws determined the full-scale representation of the test. The model had a one-inch diameter and 1.8-inch length due to the availability of previously built molds. The tunnel velocity was limited to 100 mph because the

lasers were mounted inside the tunnel. At 100 mph, there was noticeable buffeting of the lasers, and it was decided not to increase tunnel velocity to the 138 mph required for Froude scaling.

Table 3 shows the two test cases compared against the Froude scaling requirements for a Mk-81 at 5% scale in the AFIT low speed wind tunnel. The use of pre-existing molds prevented model dimensions from matching Froude requirements. Additional molds could have been designed in a CAD program and built using the Rapid Prototype (RP) printer; however, it was decided to use the existing mold with a 1.0-inch diameter because of the increased surface area for reflecting points. The models had a 1.0-inch diameter and 1.8-inch length.

**Table 2. Tests compared against Froude scaling requirements**

	Diameter (in)	Length (in)	Airspeed (mph)	$\theta$ (deg)	m (lbs)	Dry ice Density (lbm/ft <sup>3</sup> )	I (slug ft <sup>2</sup> )	F <sub>EJ</sub> (lbf)	X <sub>EJ</sub> (ft)	t (sec)
<b>Froude Requirements</b>	0.45	3.7	138	0	0.022	65	?	0	0	0.112
<b>Dry ice Model (V=50)</b>	1.0	1.8	50	0	0.037	51	9.79E-8	0	0	0.114
<b>Dry ice Model (V=100)</b>	1.0	1.8	100	0	0.044	62	1.19E-7	0	0	0.114

The 50 mph test described here had a mass of 0.037 lbs., resulting in a dry ice density of  $51 \text{ lb}/\text{ft}^3$ . The 100 mph test had a mass of 0.044 lbs., resulting in a dry ice density of  $62 \text{ lb}/\text{ft}^3$ .

Each model was assumed to have uniform density for the mass moment of inertia calculations.

The test time scales matched the Froude time scale.

For easier comparison, it was important to determine the full-scale representation of actual testing capabilities. Table 3 shows the full-scale comparison. The Mk-81 has a 9-inch diameter, 74-inch length and 262 lb. mass. A Mach 0.8 release at 10,000 ft. corresponds to an airspeed of 618 mph.

**Table 3. Comparison of Froude scaling results**

	Diameter (in)	Length (in)	Airspeed (mph)	$\theta$ (deg)	m (lbs)	I (slug ft <sup>2</sup> )	F <sub>EJ</sub> (lbf)	X <sub>EJ</sub> (ft)	t (sec)
<b>Mk-81</b>	9.0	74.0	618	0	262	?	0	0	0.50
<b>V=50 Full-scale</b>	20.0	36.0	224	0	440	7.29E-3	0	0	0.51
<b>V=100 Full-scale</b>	20.0	36.0	447	0	524	8.87E-3	0	0	0.51

The scaled dry ice model corresponded to a 20-inch diameter and 36-inch length. Limited model sizes resulted in a weapon model with a large diameter. The 50 mph test corresponded to a 440 lb. weapon released at 224 mph. The velocity was expectedly low, because the tunnel velocity was purposely limited to 50 mph instead of the desired 138 mph. The 100 mph test corresponded to a 524 lb. weapon released at 447 mph. With such a large model, lower densities better matched the desired mass. The time scales were within 2% of the desired scale.

For this analysis, weapon dimensions, weight and time scale were specified while weapon attitude, ejector force and ejector location were set to zero. The weapon attitude was set to zero because it did not require scaling in each of the scaling laws used. The use of Froude scaling made the use of ejectors unnecessary. Instead, this research used a free-drop for simplicity. Therefore, the ejector location and force were zero. Because the mass moment of inertia is not publicly available for the Mk-81, it was not considered in the scaling of the model. However, the mass moment of inertia was calculated for the dry ice models and scaled up to full scale.

### **Experimental Facilities and Experimental Setup**

Testing occurred at the AFIT low-speed wind tunnel, seen in Figure 2. It is an open-circuit tunnel with an 8:1 contraction ratio [12] and a test section of 31 by 44 by 72 inches [13]. The tunnel is capable at speeds up to 65 m/s and has three-sided optical access for easy visualization. Two hinged sidewalls allow quick tunnel access. The published turbulence level is approximately 1% [12].



**Figure 2. AFIT low-speed wind tunnel**

### ***Wind Tunnel Equipment***

A clear Plexiglas section formerly used for hotwire testing replaced the ceiling of the test section. The piece has a network of 0.5-inch wide grooves cut through the 0.75-inch thick window seen in Figure 3. The slots are present to accommodate a hotwire arm. For this experiment, the generic aircraft cavity mounted to the tunnel ceiling through the slots. The unused slots were filled with temporary Plexiglas filler or taped over during testing.





**Figure 3. Wind tunnel ceiling**

The mock aircraft cavity was made of RP Material with clear acrylic sidewalls. The full model size is 2.2 inches wide by 2 inches deep by 15.3 inches long, with inner cavity dimensions of 1.5 x 1.5 x 5.0 inches, resulting in a length-to-depth ratio of 3.33, slightly less the 3.6-6.0 used in previous research [1,2,4,8,14,15]. The user designed the aircraft cavity model with smooth, rounded edges to prevent strong turbulence. The ramp angle both forward and aft of the cavity is 23.2 degrees, with rounded edges using a varying radius fillet. Each ramp has two counterbore holes drilled through to accommodate the mounting hardware. Figure 4 shows a three-view of the cavity.

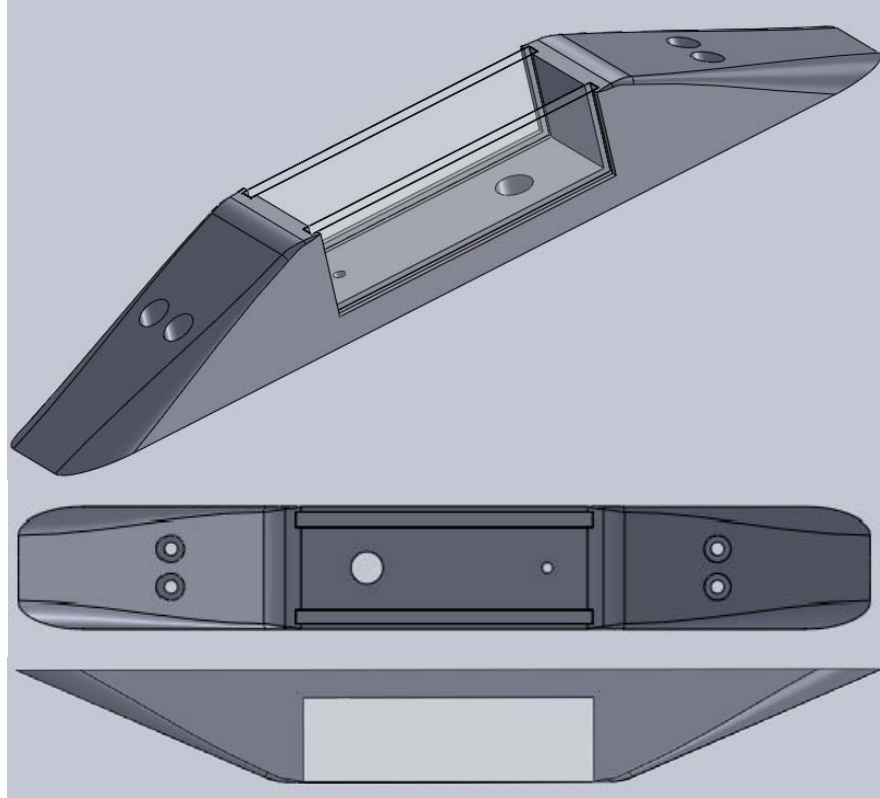


**Figure 4. Three-view of generic aircraft cavity**

The large hole in the base is 0.6 inches in diameter, allowing the release mechanism to penetrate the cavity. The small hole near the aft cavity wall would allow a pressure transducer of 0.2-inch diameter.

The release mechanism provided repeatable release conditions for the store model. As Shalaev, Fedorov and Malmuth [3] state, the flight of a store through a shear layer, aircraft boundary layer and into freestream flow depends on initial conditions. For this reason, the release mechanism attached to the frame bracing the top of the wind tunnel so the only allowable movement was to open and close.

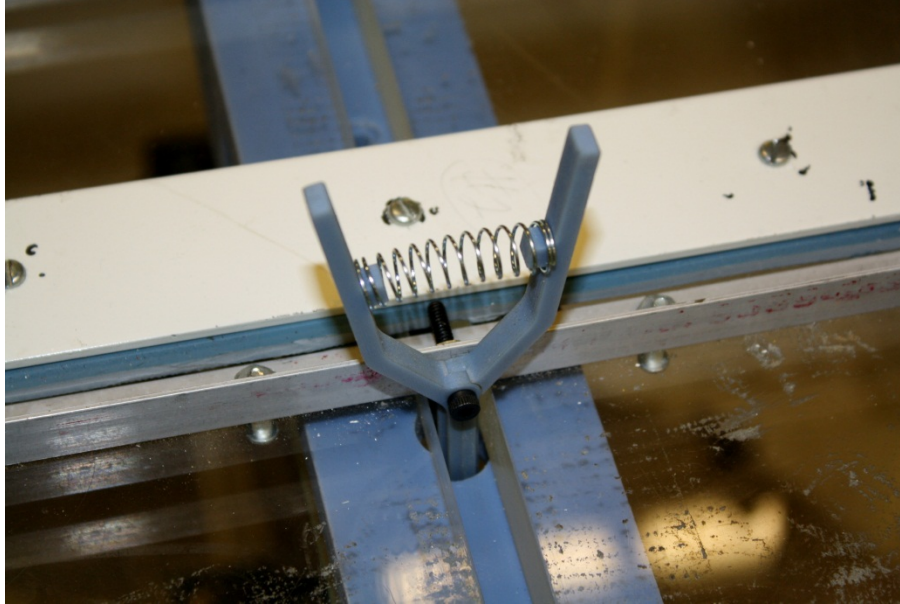


**Figure 5. Top-view of release mechanism**

A screw through the release mechanism pivot attached to the L-bracket that runs width-wise across the top of the tunnel ceiling, shown in Figure 5. The spring-loaded design allowed the user to load the model and hold it in place without manually holding it.

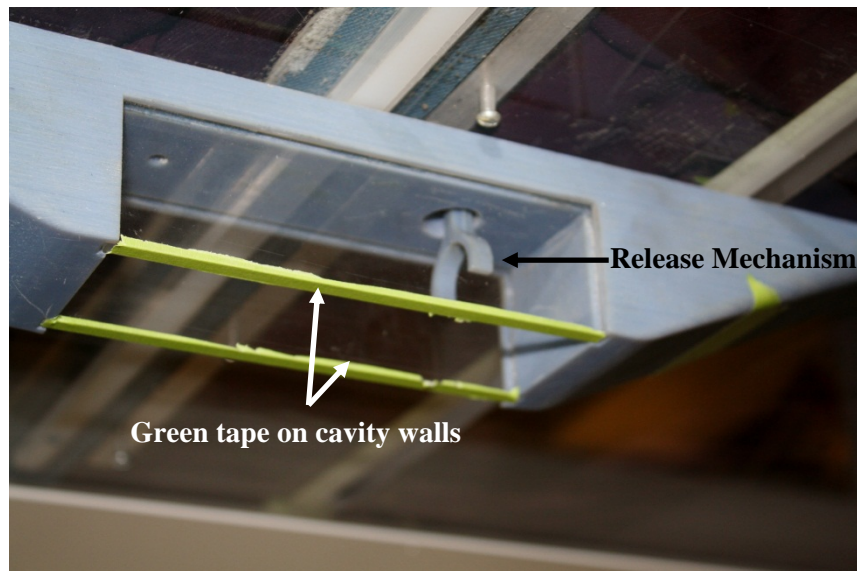


**Figure 6. Cavity-view of release mechanism**

The user pinched the mechanism arms together to load and release the model. As seen in Figure 6, the circular arms projected into the cavity to hold the model in the center of the cavity. The

strip of green tape on the end of each cavity wall provided an opaque surface from which to reflect the reference points.

### ***Wind Tunnel Operations***

The wind tunnel is an open-circuit system. The tunnel is self-contained in the lab; it does not intake or exhaust the air supply from outside. The wind tunnel is computer controlled using National Instrument's LabView software. Once the tunnel fan had been switched on, the program was opened and started. The only controls used for this research was the speed control. The tunnel took 10-15 seconds to accelerate once the user entered the desired test velocity.

### ***Cameras Used for Photogrammetry***

This research used three MotionPro X-Stream XS-4 series high-speed cameras with Nikkor lenses, like those shown in Figure 7. For ease, the user labeled the cameras as "A, B, C".

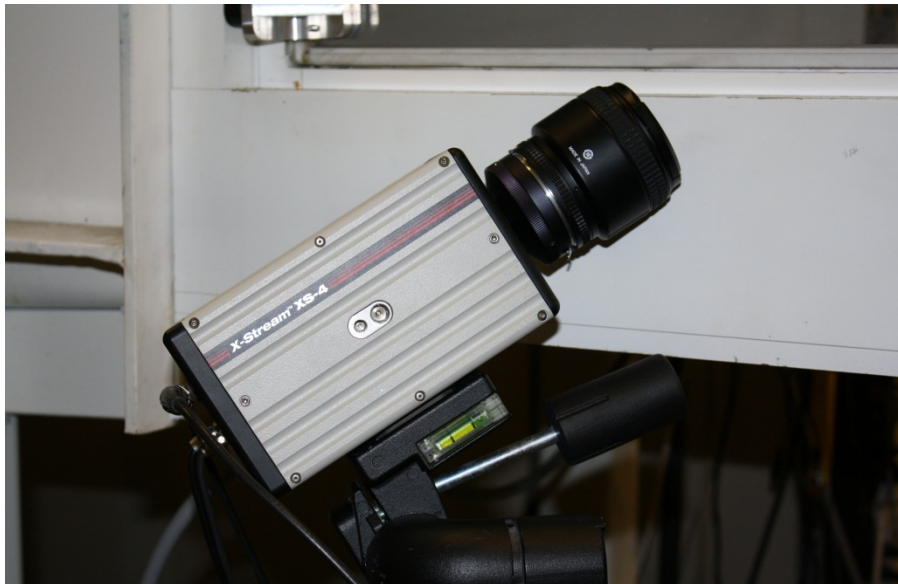


**Figure 7. The MotionPro X-Stream XS-4 cameras used. This is camera 'A'**

Cameras A and C used Nikkor 85mm lenses with an aperture of four while Camera B used a Nikkor 105mm lens with an aperture of 5.6. The low apertures cause a shallow depth of field, but were necessary to capture adequate light during the short exposures. The cameras focused on the exit plane of the cavity.

MotionPro designed the X-series cameras for use in industrial and research applications for motion evaluation. They connected to the computer via a USB 2.0 digital interface. The newest camera (camera B) could also use a Gigabit Ethernet connection. The cameras are capable of collecting 1000 full frames per second, well above the 700 frames per second used for testing. The spatial resolution of each camera is 512 by 512.

For synchronized photography, camera C was the master and cameras A, B the slaves. BNC cables connected the SYNC OUT of the master camera to the SYNC IN of the slave cameras. A “T connector” connected the two slave cameras to the master. Figure 8 shows the interface on the back of each camera. Specifically shown is camera C, as the BNC cable is connected to the SYNC OUT port.



**Figure 8. The interface on the back of each camera**

MotionPro’s Motion Studio software suite controlled the cameras, recorded, and manipulated the images. Figure 9 shows the Motion Studio record menu. Shown is the option to designate the master camera.





**Figure 9. The option to designate master camera**

Once selected for one camera, Motion Studio blocked the option for the other cameras. Changing master camera options automatically changed the slave options accordingly. Figure 10 shows the default software settings.

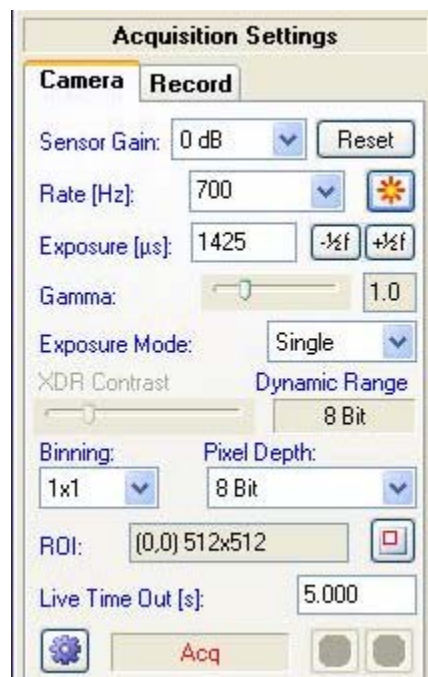


**Figure 10. Default camera settings**

For this research, the shutter speed was set to 700 Hz, with a 997  $\mu$ s exposure. The record mode was set to normal, and the cameras recorded 3500 frames per test to ensure the video captured the store release. Only the frames showing model movement were used in data processing. Each camera had the same menu options.

### ***Camera Test Setup***

All three cameras connected to the computer using USB 2.0 cables. To achieve the desired exposure time, the shutter speed was set to 700 Hz, with a 997  $\mu$ s exposure at an f-stop of

4 and 5.6, as discussed above. This provided adequate contrast to view the laser grid and the moving model. The cameras were placed clockwise around the tunnel alphabetically. Camera A (serial number 1412050046) was positioned on the left, downstream side of the tunnel. It is the left-most camera seen in Figure 11.



**Figure 11. Cameras A and C**

Camera C (serial number 1404050016) was located on the left side of the tunnel, upstream from the cavity. It is the right-most camera in Figure 11. Camera B (serial number 1416080507) was located on the right side of the tunnel, centered on the cavity. It is seen in Figure 12.



**Figure 12. Camera B and the computer used to control cameras**

These camera locations achieved 360-degree coverage of the cavity. For the software to determine the 3-D location of each point, it must be visible by at least two cameras. Increasing the number of common points between the three cameras increases the software's ability to create an accurate 3-D representation.



**Figure 13. Top-Down view of camera setup**

The sheet seen in Figure 13 covering the wind tunnel ceiling protected the individual on the ceiling from the lasers. While this research only used 5mW lasers, it was important to protect the individual from the distraction of low-power laser light.



### ***Laser Grids***

The lasers used in this research were 5mW, class IIIa, lasers in the 600-710 nm wavelength range. Each laser was fitted with a matrix projector head that split the beam into a 7 by 7 array of points. The grid focused on the store surface with additional points projected on the cavity acting as stationary targets during image processing. The green tape visible on the cavity wall ends in Figure 14 allowed adequate reflection of the laser dots defining the cavity while maintaining clear walls for camera visualization of the model both inside and outside the cavity.

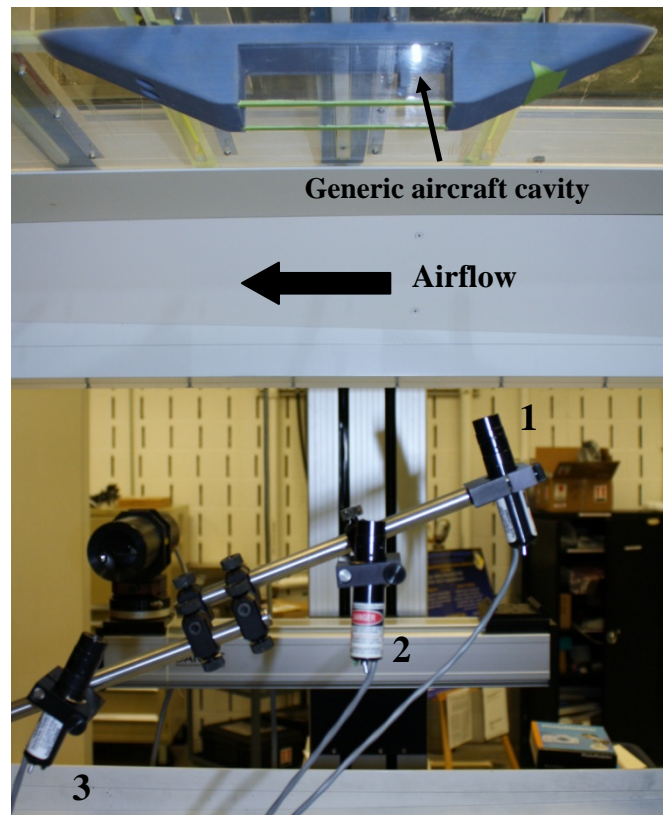


**Figure 14. Side profile of laser setup**

Three laser generators marked the test area, as shown in Figure 14. The wind tunnel sting projected the lasers into the test section, which could influence the flow around the cavity. However, it was determined the effect of the laser sting was minimal as they were all mounted away from the cavity. Laser one was mounted on the front end of the sting, 7.5 inches below and 2.0 inches in front of the release point. Laser two was mounted 10 inches directly underneath the

release point. These two lasers marked points on the tunnel walls as well as the model. The third laser, 13 inches below and 8 inches behind the release point, only marked the model as it moved from the cavity. Reference points are the unmoving laser dots on the cavity walls used to define the coordinate system. Marker points are the laser dots on the model surface used to define the location and curvature.

### ***Fabrication of Dry Ice***

Dry ice is commercially available and has been most commonly used for refrigeration and special effects. With the sublimation temperature of 194.65 K at one atmosphere and relatively fragile construction, it offered the possibility of being formed into models for wind tunnel experiments without causing serious risk to tunnel components.

The fabrication method used for this research was based on the process used by Kohlman and Richardson [10], who formed the model by directly injecting liquid carbon dioxide into a mold. Callaway [9] further refined this process and has a full discussion on the background and the development of the method described below. The general principal was to flash freeze carbon dioxide by quickly reducing the pressure from 350 psig to ambient conditions.

Testing used a Dewar 300-350 psig carbon dioxide tank because it allowed longer model production and a greater number of models per tank. Under normal circumstances, a Dewar tank produced about 40 models of the size used for testing [9].

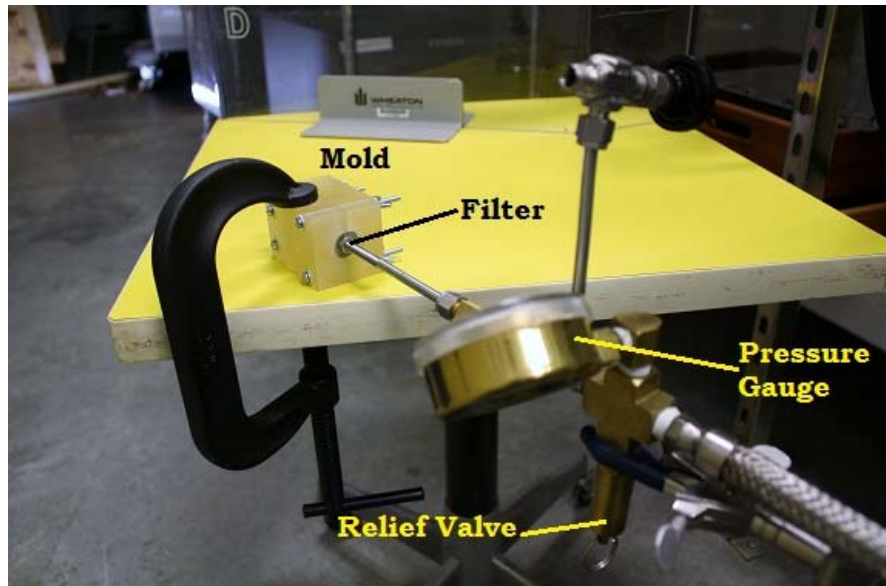


**Figure 15. Mold on the fill tube**

As shown in Figure 15, the base of the dry ice model formed against a hydrophobic metallic filter used to allow out gassing, but preventing the flow of liquid carbon dioxide from the mold. Mott Corporation produced the filters out of 316L stainless steel [9]. The filter porosity ranged from 0.1 to 100 microns, with this research using a 20 micron filter because Callaway found this produced the highest quality 1.0-inch diameter models in his previous research.

Testing used molds built as part of Callaway's research. They were made of RP material and showed no sign of wear after repeated tests. The mold was in two pieces, held in place by four screws, seen in Figure 15. The user drilled three 0.046-inch diameter vent holes through each half of the mold to help fill imperfections, similar to casting. Model quality noticeably improved, but the success rate also dropped. Before the vent holes, it was estimated 60% of the models were successfully produced. After, it was estimated only 33% were successfully produced. The vents may have caused the pressure in the mold to decrease too much, allowing the CO<sub>2</sub> to freeze prior to reaching the mold.

The process was not exactly the same as that used by Callaway. First, he scaled down to a 0.6-inch diameter base because of problems achieving supersonic flow with the 1.0-inch diameter models. This research used the 1.0-inch diameter models to maximize the number of

marker points on the surface. In addition, the user had to remove the dry ice model from the feed tube before loading it in the tunnel. An acrylic plug insulated the dry ice model from the metal feed tube. This plug was shortened to 0.25-inches and smoothed to aid in model removal. This resulted in a small void in the aft end of the model.

Working with high-pressure cryogenics required the use of basic safety measures. A 130 psig pressure relief valve was connected the feed line to prevent over-pressurization of the mold. A manual relief valve relieved pressure after turning off the liquid CO<sub>2</sub>. A 500 psig pressure gauge displayed feed line pressure, which aided in fabrication because 300 psig builds dense models. It also allowed the user to ensure the line was not building excessive backpressure. In addition, a C-clamp secured a safety shield to the table. Goggles and gloves were worn during fabrication and handling of the model.

Drop tests only used models with minimal surface defects. Accurate tracking required a smooth surface to reflect the lasers. Small rough patches in the model surface were somewhat common.



**Figure 16. Dry ice fabrication setup**

For model fabrication, a single flexible metal hose connected the Dewar's liquid tap to the mold and its pressure gauge and pressure relief valve, shown Figure 16. A C-clamp secured the mold to the table to prevent movement during fabrication or during the pressure relief valve exhausting. The tank has a pressure-building tap to maintain Dewar pressure between 300 to 350 psig during testing. Care had to be taken from rapidly producing models so the Dewar was not overdrawn and components did not clog. A handheld heat gun kept the hose and joints from freezing.

### **Test Procedure**

Each test required two people, although three was preferred. One person released the store, one monitored and controlled the cameras and one monitored and controlled the wind

tunnel. Two people could run the experiment if one person controlled both the wind tunnel and the cameras.

The process for model fabrication is as follows. The user gradually opened the liquid tap on the Dewar one-half of a turn. Once liquid flow reached the model, visible by a milky cloud, the user opened the tap another full turn to force the pressure rise needed for high quality models. The transparent nature of the model allowed easy viewing. Once the pressure gauge read at least 300 psig, the user closed the valve and removed the model from the mold to examine for defects.

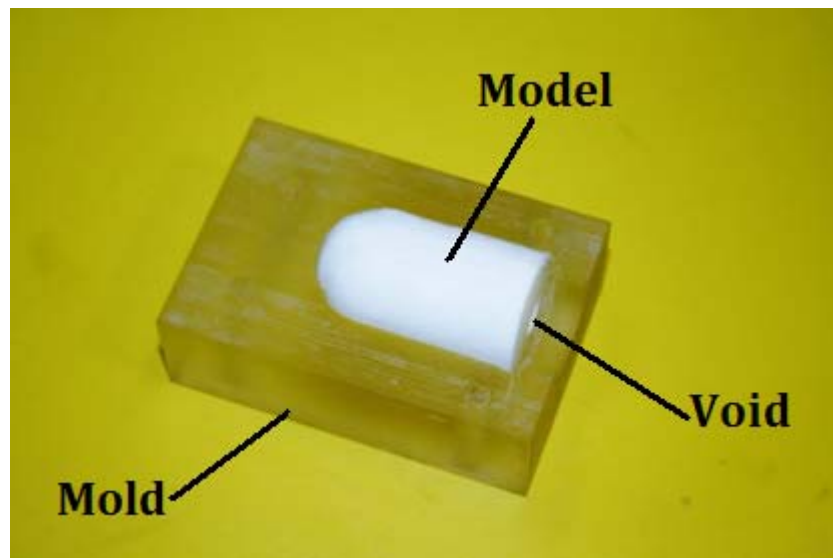


**Figure 17. Completed dry ice model**

Figure 17 shows a completed model in the mold. The small void is visible where the feed tube once projected into the model. This was a successful model because there are minimal surface defects.

Once a model was successfully built, it was inserted into the test section. As one person opened the release mechanism, the other, wearing protective gloves, loaded the model in the cavity. Once loaded, the tunnel doors were shut and the desired tunnel velocity set. Freestream velocity was set to zero for a control case. For store separation modeling, airspeeds of 50 mph and 100 mph were used in the tunnel. One individual monitored the test section while the tunnel fan accelerated. Once up to speed, the user manually triggered the cameras and the store

released. The tunnel velocity was set back to zero moments later. The time from model build completion to release was approximately one minute. During this time, the model underwent sublimation. In fact, the resulting fog provided easy visualization of the vortices shed from the leading edge of the cavity. Nevertheless, the dimensions of the released model were close to the prescribed value. PhotoModeler® imported and processed the images to create a 3-D model, as discussed below.

This process required good communication over the noise of the tunnel. The two or three individuals constantly communicated to make sure each test was successful. A failed test occurred when the cameras did not capture the model release.

### ***Image Data Capture***

As discussed in this paper, a frame is an individual image set captured by the high-speed cameras. An epoch is a single image set in PhotoModeler® used to create a 3-dimensional representation of the model location and orientation at a given time. While each test captured 3500 frames, PhotoModeler® only analyzed 21 epochs. For the zero mph calibration test, every third frame was loaded into PhotoModeler® and analyzed, creating 21 epochs. For the 50 mph and 100 mph tests, every fourth frame was loaded into PhotoModeler® and analyzed, creating 21 epochs.

Stereo-photography captured the laser grids projected on the store and cavity surfaces. Testing used PhotoModeler®, a commercially available software package used to produce three-dimensional models from photographs. The software can use images from virtually all sources, whether from cameras calibrated in PhotoModeler® or cameras with known specifications. For curved surfaces, three orthogonal cameras are preferred. According to the software developer, the program is for use in areas such as accident reconstruction, architecture, preservation, archeology, forensics, film, games, animation production, and modeling for engineering, industrial and experimental applications.

The PhotoModeler® Video (PMV) captured the model movement between epochs. The module loads image sequences and automatically tracks target points through time to increase user efficiency [14]. For all imagery, the user defined which frame corresponded with  $t_o = 0$ . There was no automatic trigger to begin image capture as the release mechanism opened. The user needed to inspect the images manually, ensuring accurate target tracking. Figure 18 shows the images from each camera with marked points. PhotoModeler® generated three-dimensional coordinates for each point.

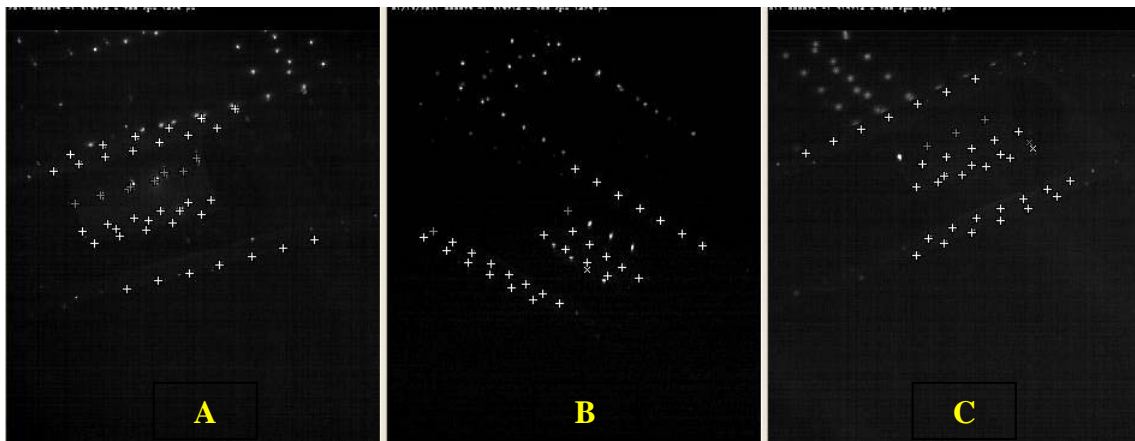


**Figure 18. Example of three images captured**

After image acquisition, the user correlated the three images using common points referenced in each photo. Points had to be marked in at least two photos to be referenced. The number of common points needed for correlation depended on the camera angles and the number of points in each photo. The reference points on the cavity walls provided a stationary reference frame. The (x, y, z) location of the marker points could then be determined. For ease, only the reference points were used to correlate the images. From these points, PhotoModeler® calculated the location of each camera in relation to the cavity and built the three-dimensional space.

With correlated images, the marker points on the model surface needed to be linked. PhotoModeler® predicted the position of the expected point, which revealed the quality of the three-dimensional correlation.



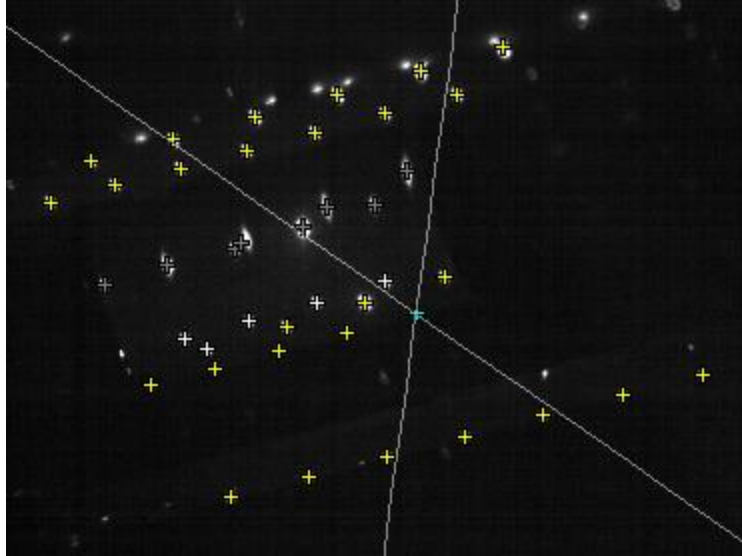


**Figure 19. PhotoModeler® triangulating the expected location of a point**

If the expected point location was off by more than a few pixels, the correlation was poor and the photos needed to reprocess. In Figure 19, PhotoModeler® triangulates the expected position of a point in the third image given its location in the first two.

The user needed to check the residuals after completely referencing the images in the first frame. The residual is a measure of disagreement between the cameras about the location of a point in three-dimensional space. Lower residuals indicate a quality setup, images, and point identification. PhotoModeler® automatically identified points with high residuals so the user could fine-tune point location. Once reaching an acceptable residual, PhotoModeler® propagated through the sequence of images. The user inspected each image manually to ensure correctly referenced points and low residuals.

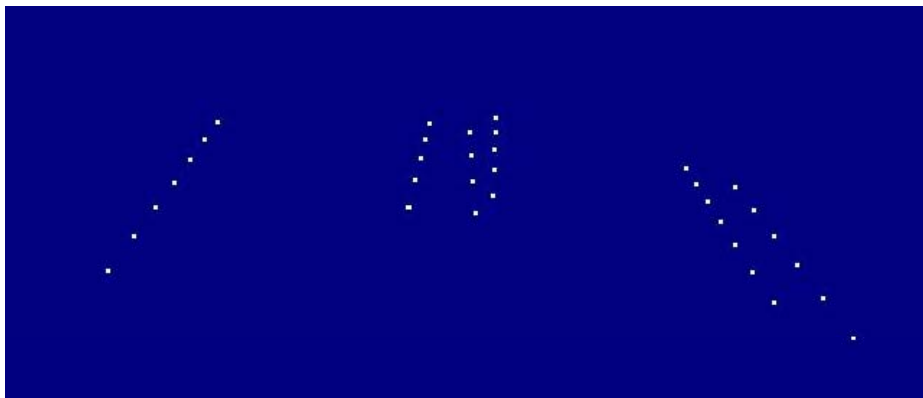


**Figure 20. Three-dimensional model created by PhotoModeler®**

Figure 20 shows a rendered three-dimensional model based on the provided images. The model can be rotated and viewed at each time step processed. PhotoModeler® exported the coordinates of the point cloud in a text file.

Table 4 shows the locations of point 1000 for each epoch of the 50 mph test. Point 1022 was one of the reference points on the cavity wall used to define the coordinate axis. Point 1022 moved less than 0.01-inches through the whole test, which validated the assumption of a stationary reference frame. The fourteen reference points needed to move as little as possible to resolve the store model accurately.

**Table 4. Locations for reference point (Point 1022) on the cavity**

Point ID	Epoch Number	X [inches]	Y [inches]	Z [inches]
1000	0	0.000	-1.600	0.000
1000	1	0.001	-1.600	-0.003
1000	2	0.005	-1.600	0.000
1000	3	0.006	-1.600	-0.001
1000	4	0.009	-1.601	-0.001
1000	5	0.009	-1.602	0.000
1000	6	0.010	-1.600	-0.002
1000	7	0.009	-1.601	0.000
1000	8	0.003	-1.602	-0.001
1000	9	0.004	-1.599	-0.002
1000	10	0.001	-1.599	-0.003
1000	11	0.002	-1.600	-0.001
1000	12	0.002	-1.600	-0.001
1000	13	0.000	-1.600	0.001
1000	14	0.000	-1.600	0.001
1000	15	0.003	-1.600	-0.001
1000	16	0.001	-1.599	0.002
1000	17	0.001	-1.599	0.002
1000	18	0.001	-1.600	-0.006
1000	19	0.001	-1.599	-0.005
1000	20	0.005	-1.599	-0.001

## Limitations

Due to the high point density on the model surface, the automated tracking software built into the PhotoModeler® PMV module could not accurately process multiple frames at once. Due

to the curved surface of the model, points could move large distances between epochs. Likewise, the model's movement through a stationary laser grid caused new points to appear and disappear. Finally, having multiple laser sources caused points to intersect and cross paths. The first problem can be overcome by recording images at a higher frequency, which then yields more photographs needing processing. The other problems required significant user input. Each frame had to be inspected manually to ensure each point label was consistent. Depending on the number of points in each image and the amount of model movement, this could take between 10-25 minutes per epoch.

## IV. Results and Analysis

### Raw Imagery

For easy visualization, the first and last frames processed for each camera are shown. The only easily seen light is that of the reflected laser grid. The high contrast between the dark background and the bright points allowed easy marking. PhotoModeler® used many of the points visible in each row to create the 3-D model.

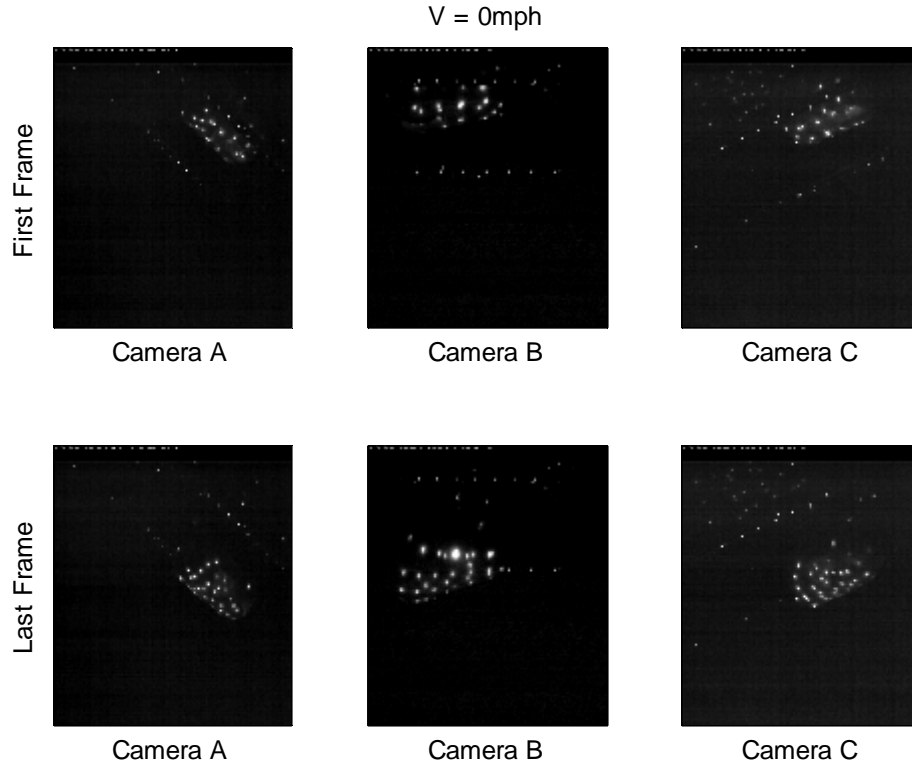


**Figure 21. First and last frames processed of each camera at  $V_{\infty} = 0 \text{ mph}$**

The first row of images corresponds to the first epoch, at  $t = 0.00$ , processed for the test. The second row corresponds the last epoch processed for the test. The model occupies the upper quadrant of each photo, allowing room in the focal plane for the model to fall away. To create a smooth moving model, every third frame captured by the high-speed cameras was processed. As a result, the time between epochs is 0.0043 seconds. As seen in Figure 21, processing could have continued because the laser dots were still in focus in each image. However, time constraints

prompted a termination of image processing for this test. Further processing utilized every fourth frame, at a 0.0057-second interval, to save time. Twenty-one epochs modeled the motion for 0.0858 seconds, which corresponds to 0.384 seconds at full scale, below the goal of 0.5 seconds.

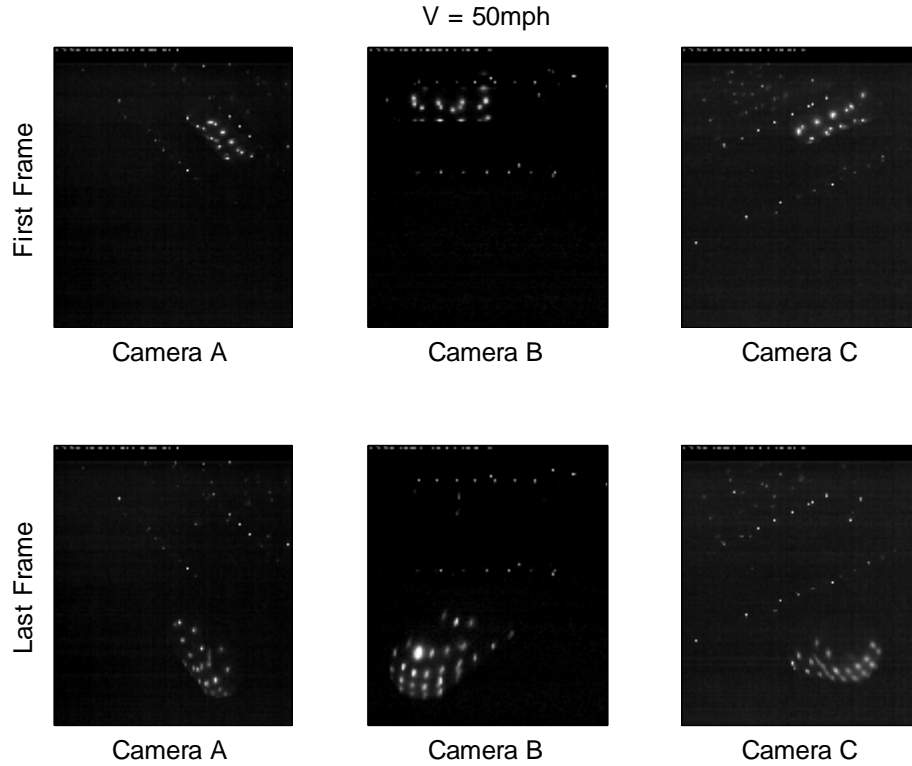


**Figure 22. First and last frames processed of each camera at  $V_{\infty} = 50 \text{ mph}$**

The second test was at a freestream velocity of 50 mph. Again, the model in the first frame is in the upper quadrant of each image. For this test, the user processed every fourth image, at a 0.0057-second interval. As seen in Figure 22, the model is beginning to move out of focus of camera B. The laser points must be in focus for accurate marking. The view from Camera B shows the model with a distinct nose-down attitude. Without any control surfaces, the model will continue to nose-down and begin to tumble down the wind tunnel. Twenty-one epochs modeled the motion for 0.1143 seconds, which equates to 0.511 seconds at full scale, exceeding the goal of 0.5 seconds.

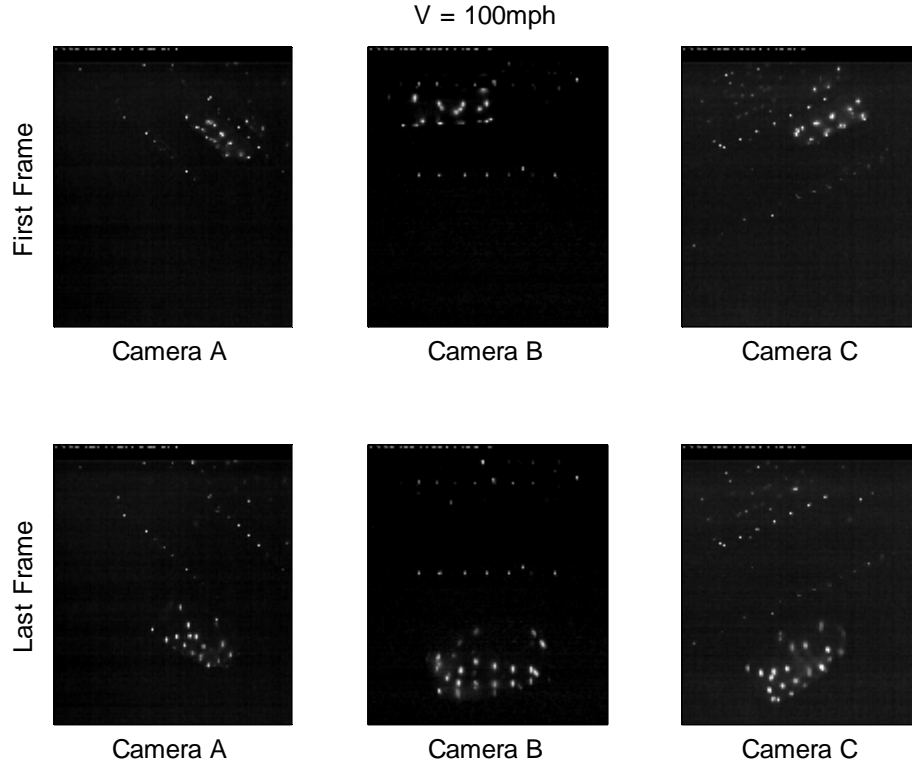


**Figure 23. First and last frames processed of each camera at  $V_{\infty} = 100 \text{ mph}$**

The third test was at a freestream velocity of 100 mph. Again, the model in the first frame is in the upper quadrant of each image. For this test, the user processed every fourth frame, at a 0.0057-second interval. As seen in Figure 23, the model is near the image boundary. Twenty-one epochs modeled the motion for 0.1143 seconds, which equates to 0.511 seconds at full scale, exceeding the goal of 0.5 seconds.

There are enough points to reproduce models with a reasonable level of accuracy. Increasing the number of cameras would improve model accuracy because of the corresponding increase in common points.

A handheld camera recorded a single 100 mph test for qualitative analysis. Figure 24 shows the six useful frames from the video that show the model movement. The user defined  $t_0$ . The frame rate was 30Hz, much lower than the 700Hz from the high-speed cameras. While the

images are very blurry, they provide an understanding at the speed at which these dry ice models move. The red laser dots are seen on the model and cavity walls.

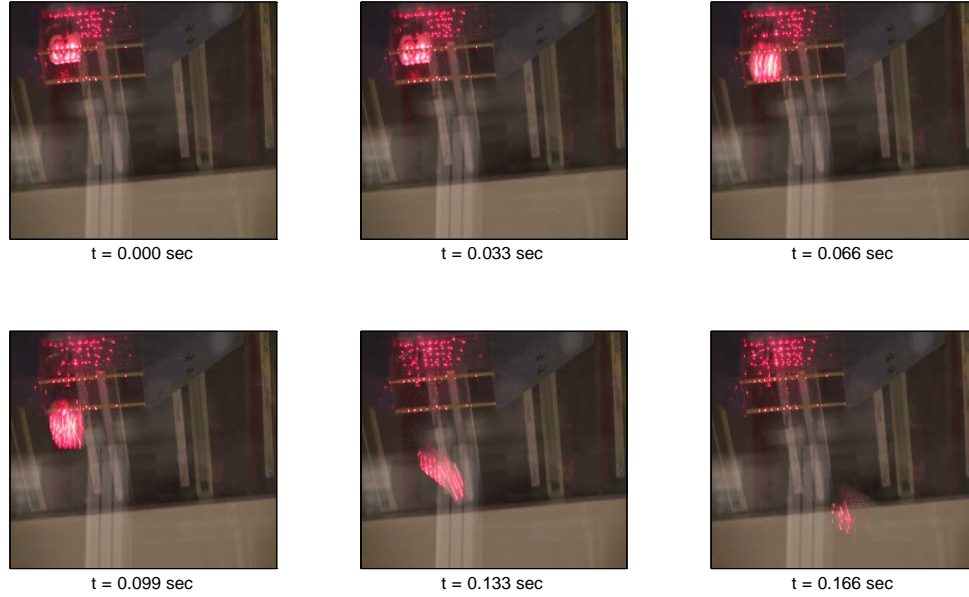


**Figure 24. Frames from handheld camera.  $V_{\infty} = 100 \text{ mph}$ .**

Here in Figure 24, the freestream flows from left to right. The handheld camera, located near camera B, viewed the store from below. In this visualization, the first two frames ( $t = 0.000$ ,  $t = 0.033$ ) show the first phase of separation. The model has fallen from the release mechanism but has not reached the shear layer. In the third frame ( $t = 0.066$ ), the model is crossing through the shear layer, the second phase of separation. In the fourth frame ( $t = 0.099$ ), the model enters the tunnel freestream. It is clear in the fifth frame ( $t = 0.133$ ) the model has a distinct nose-up attitude. Only a pink cloud is visible in the last frame ( $t = 0.166$ ) because of the rapid model movement. The model continues to move down due to gravity and downstream due to the freestream flow. The high-speed cameras lose sight of the store model by  $t = 0.12$  seconds. The handheld, with a larger field of view, shows the model accelerating downstream the tunnel.

## Single Point Comparison

Comparing the vertical position of a single marker point on the model surface through each test provides a quick comparison. PhotoModeler® tracked each point on the main model body for at least 14 epochs. Figure 25 shows the comparison of these points against a theoretical line, which considers only gravity.

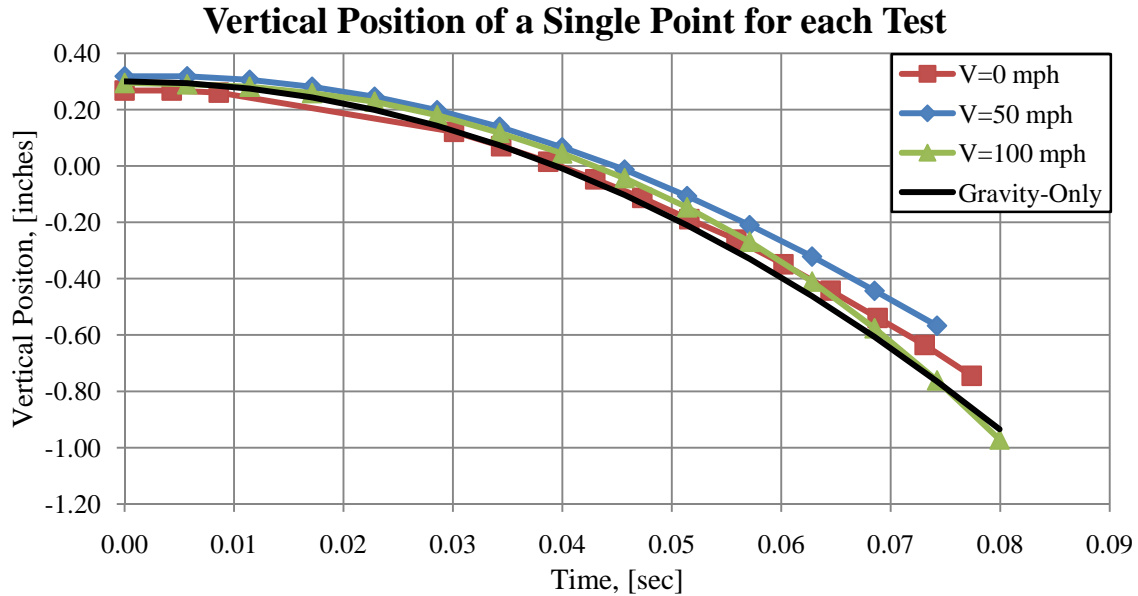


**Figure 25. Vertical position of the model for each test.**

All three experimental lines are approximately the same shape as would be expected due to gravity. The 0 mph line should match the gravity line because only gravity has a dominant effect on the model. The tests at 50 and 100 mph have the additional aerodynamic forces. The models released at 0 mph and 50 mph had a noticeable nose-down attitude, which could affect the accuracy of this data. With a nose-down attitude, the points would appear to shift in the vertical direction as they move aft on the model, causing a slower measured descent rate. The model released at 100 mph fell level for the first 16 epochs, suggesting the vertical position data should be more accurate. Because PhotoModeler® tracks the point locations, not the model itself, no single point can accurately relate the model location, velocity, or orientation. However, this single point comparison provides a brief look at the relationship between experimental results and



the theoretical outcome. All errors between the theoretical gravity line and the experimental data are less than 0.01 seconds. Considering all points on the model surface provide a more accurate measure of model location.

### PhotoModeler® 3-D Models

The PhotoModeler® results are below. All figures are labeled with their test velocity, epoch number and time stamp. For the first test, PhotoModeler® processed every third frame to create the moving three-dimensional models. For the second and third tests, PhotoModeler® processed every fourth frame to save time without any appreciable loss to model accuracy. Testing occurred at  $V_\infty = 0, 50$  and  $100$  mph. The epochs taken for comparison here are 1, 6, 11, 16 and 21. Each figure presents the model using the wind axis coordinate system.

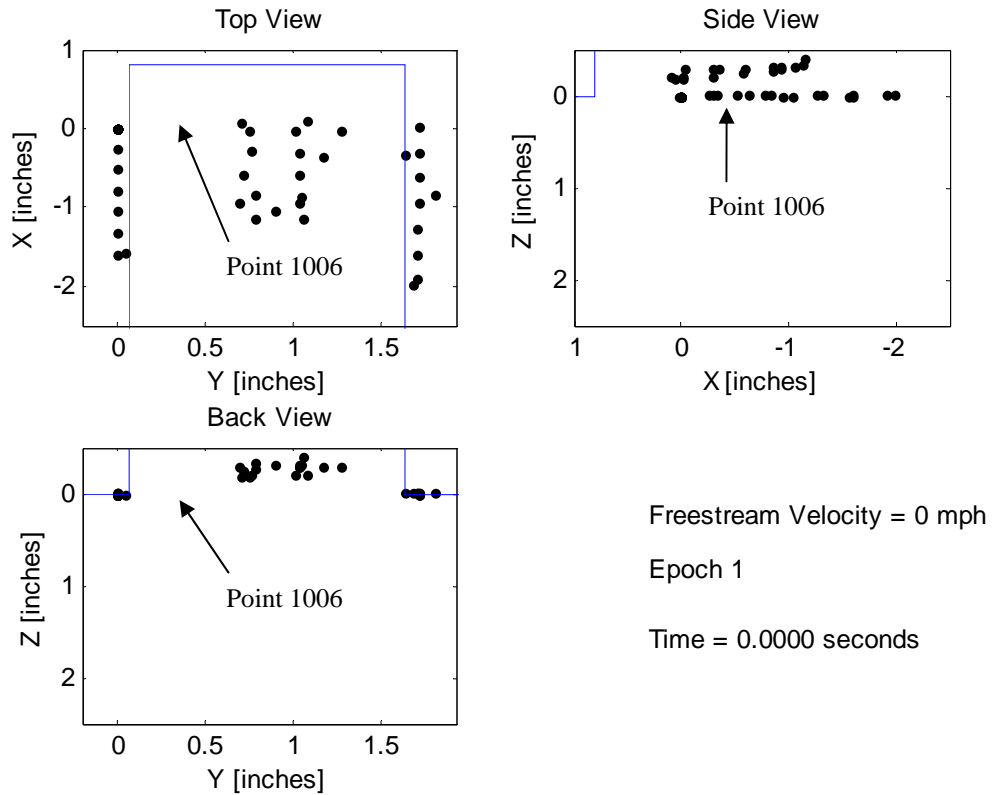


**Figure 26. Three-view of PhotoModeler® output. Epoch 1,  $V_\infty = 0$  mph**

The solid blue lines in each figure define the cavity geometry, providing a reference for model location. The first epoch of each test defined the coordinate system and scale. There were seven reference points projected on the edge of each cavity wall. As seen in the top-view in Figure 26, the reference points were the seven points in a vertical line outlining the cavity geometry. An additional three points were also visible in this epoch, bringing the total number of reference points to seventeen. Point 1006 is the origin for all imagery presented here. The two lines of reference points were 1.715 inches apart. PhotoModeler® only used points common to at least two cameras to define the three-dimensional model. Epoch one of the  $V_\infty = 0$  mph test had seventeen marker points defining the model at time,  $t = 0.00$  sec.

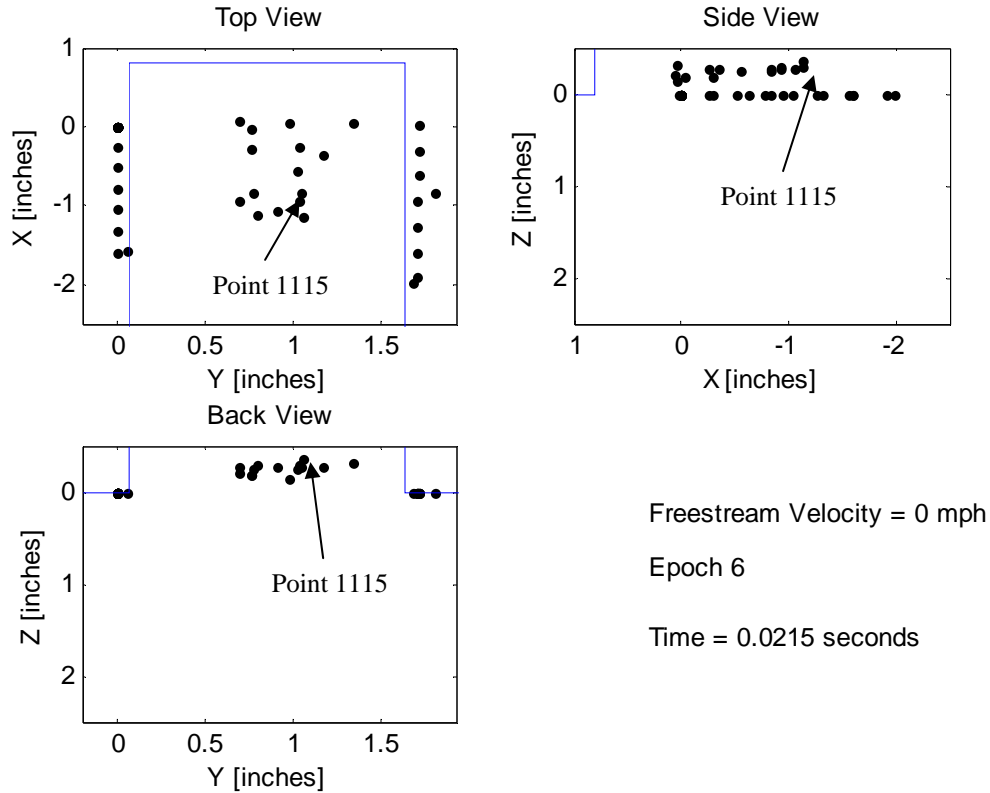


**Figure 27. Three-view of PhotoModeler® output. Epoch 6,  $V_\infty = 0$  mph**

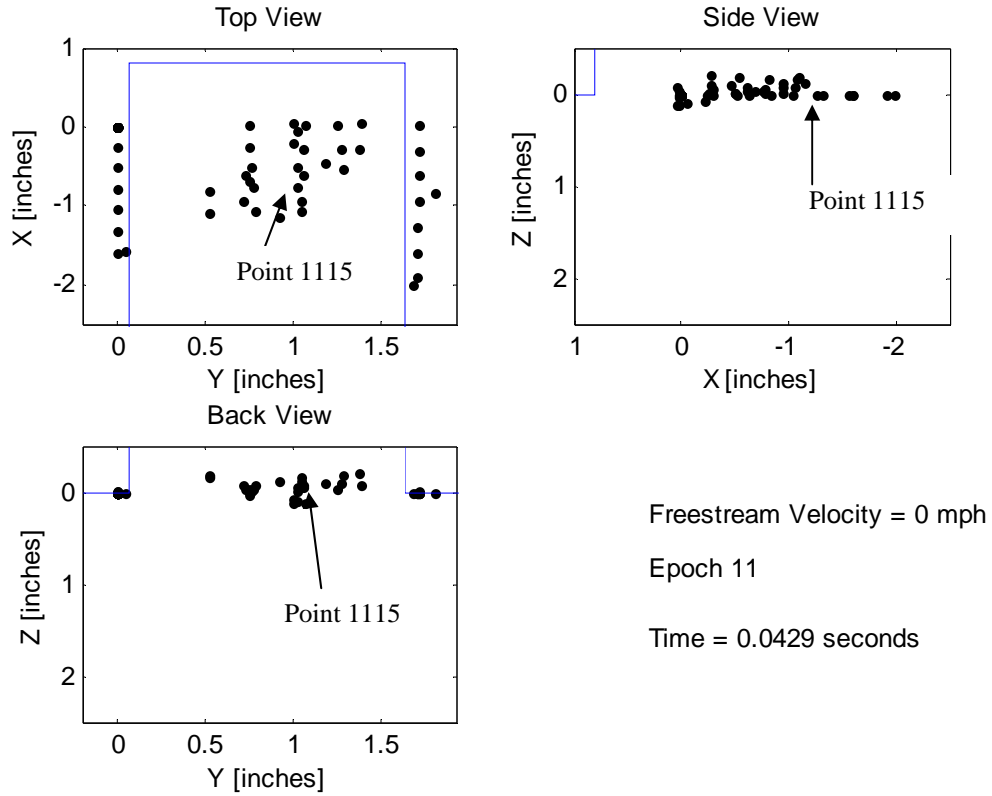
The axis system and scale defined in the first epoch carried through the remaining epochs. Although the movement is not obvious in Figure 27, the model has begun to fall from its original location in the cavity. There were seventeen reference points and fifteen marker points

defining the model. All three cameras imaged the fifteen marker points along the bottom of the model.

**Table 5. Location of a marker point (point 1115) for six consecutive epochs**

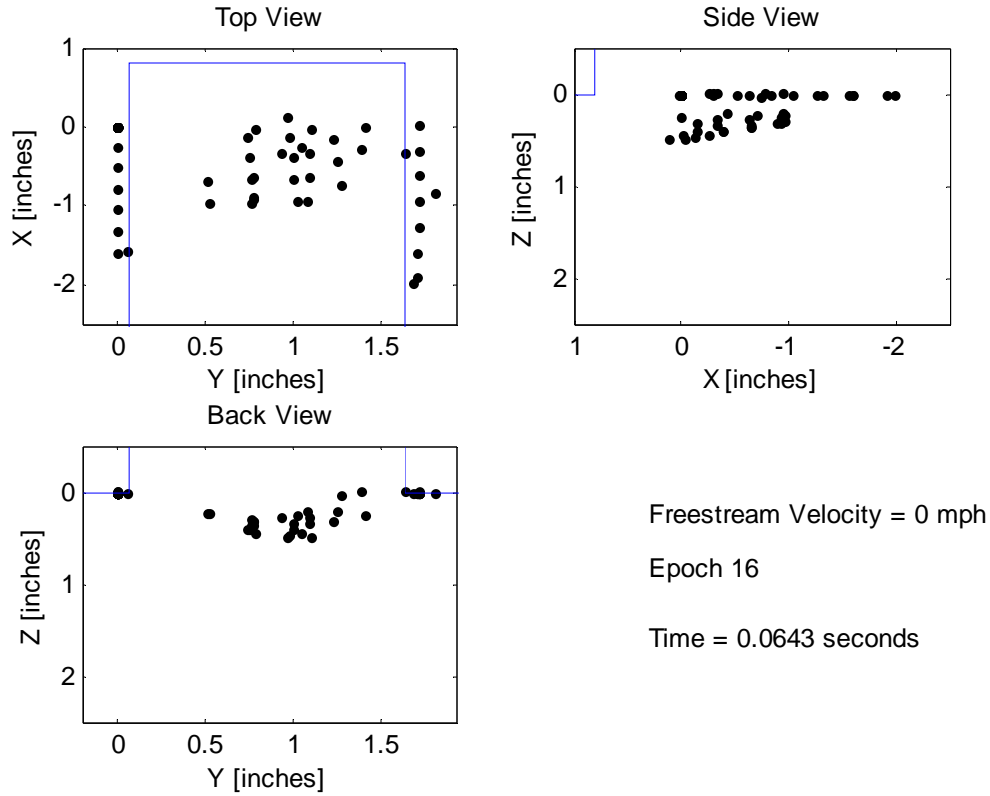
<b>Point ID</b>	<b>Epoch Number</b>	<b>Time [sec]</b>	<b>X [inches]</b>	<b>Y [inches]</b>	<b>Z [inches]</b>
1115	6	0.0215	-0.9305	0.695	-0.2763
1115	7	0.0258	-0.9327	0.6953	-0.2502
1115	8	0.0301	-0.9341	0.7001	-0.2151
1115	9	0.0344	-0.9354	0.7038	-0.1771
1115	10	0.0387	-0.9394	0.7099	-0.1281
1115	11	0.0429	-0.9404	0.7179	-0.0716

The data exists to create figures for every epoch PhotoModeler® processed. However, for the sake of brevity only a selection is displayed. Table 5 shows the (x, y, z) location and time stamp of point 1115 from Figure 27 to Figure 28. PhotoModeler® tracked each point through the test. Because an epoch corresponds to every third frame for the 0 mph test, the raw data exists to track the model location and orientation three times faster than presented here.



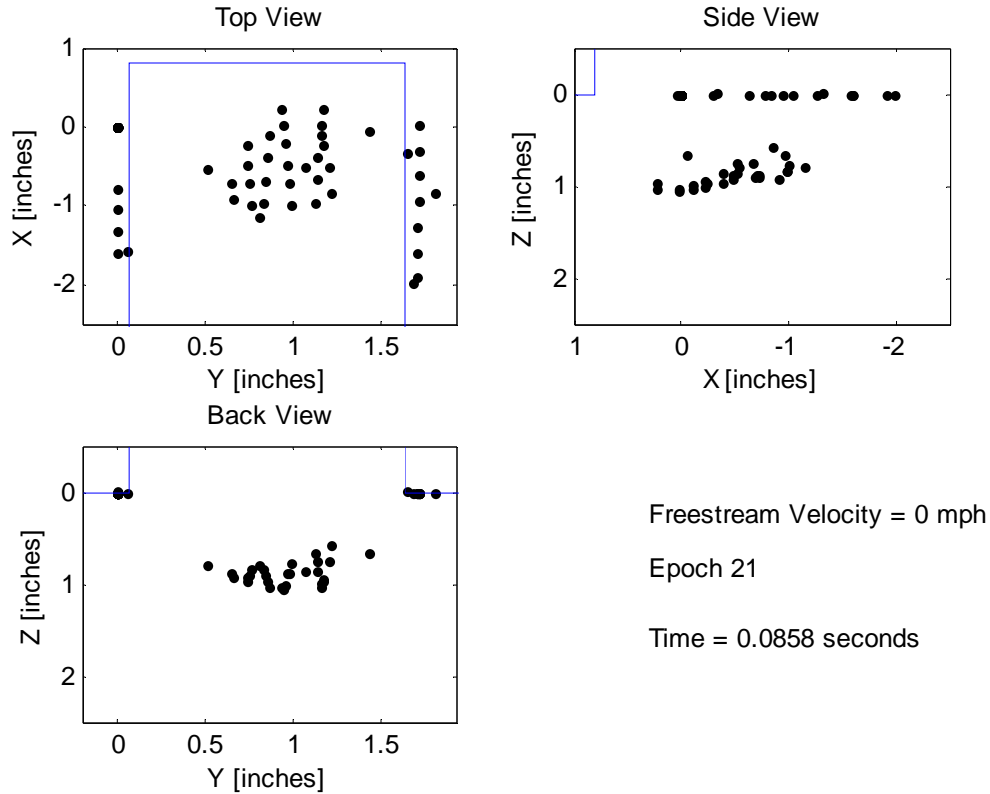
**Figure 28. Three-view of PhotoModeler® output. Epoch 11,  $V_{\infty} = 0 \text{ mph}$**

Epoch 11, seen in Figure 28, had seventeen reference points and twenty-seven marker points defining the model. Two factors could explain such an increase in the number of marker points. First, the point density increased as the model moved closer to the laser sources. In addition, marker points were visible on the sides of the model. The increased number of marker points better defined the curvature of the model, which exited the cavity with a slight nose down attitude. The model attitude itself was not critical to this research, but the ability to determine the model's attitude.



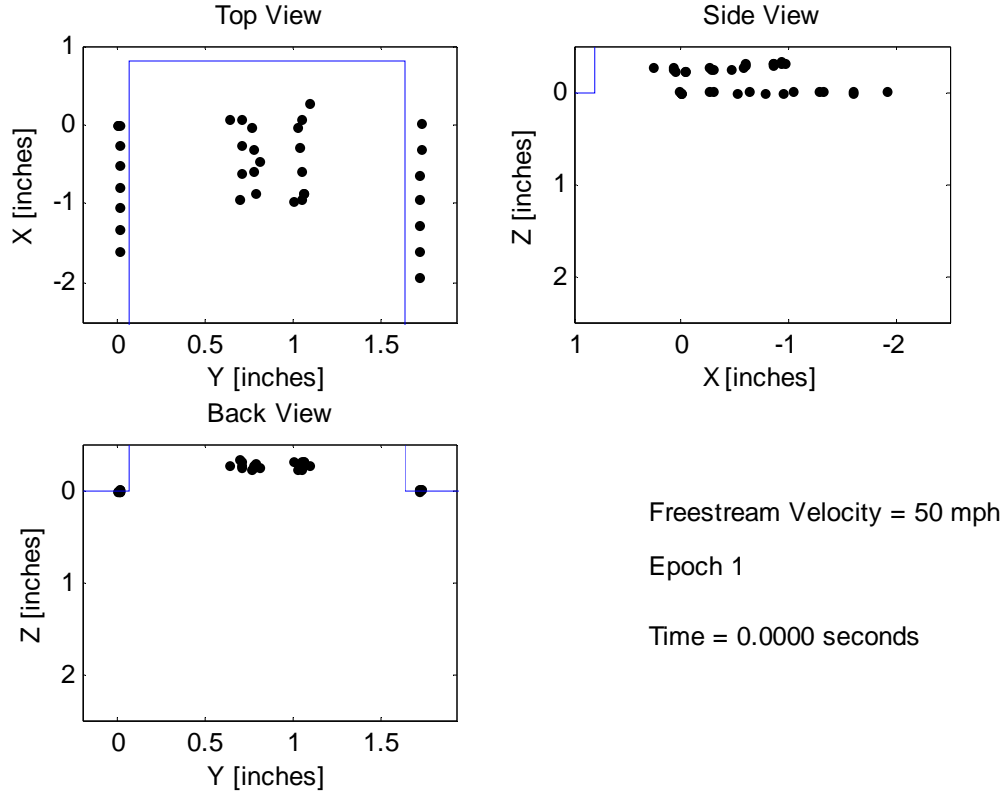
**Figure 29. Three-view of PhotoModeler® output. Epoch 16,  $V_{\infty} = 0 \text{ mph}$**

Epoch 16, seen in Figure 29, had eighteen reference points and twenty-five marker points. At time,  $t = 0.0643$ , the model was in phase two of the separation process. The model was crossing through what would be the shear layer. The side-view provides a good look at the nose-down attitude for this particular test. PhotoModeler® did not reproduce the nose of the model in this epoch. Due to the camera locations, many of the marker points on the nose were only visible by Camera C. Changing camera locations would better model the nose cone, but at the cost of modeling the store body.



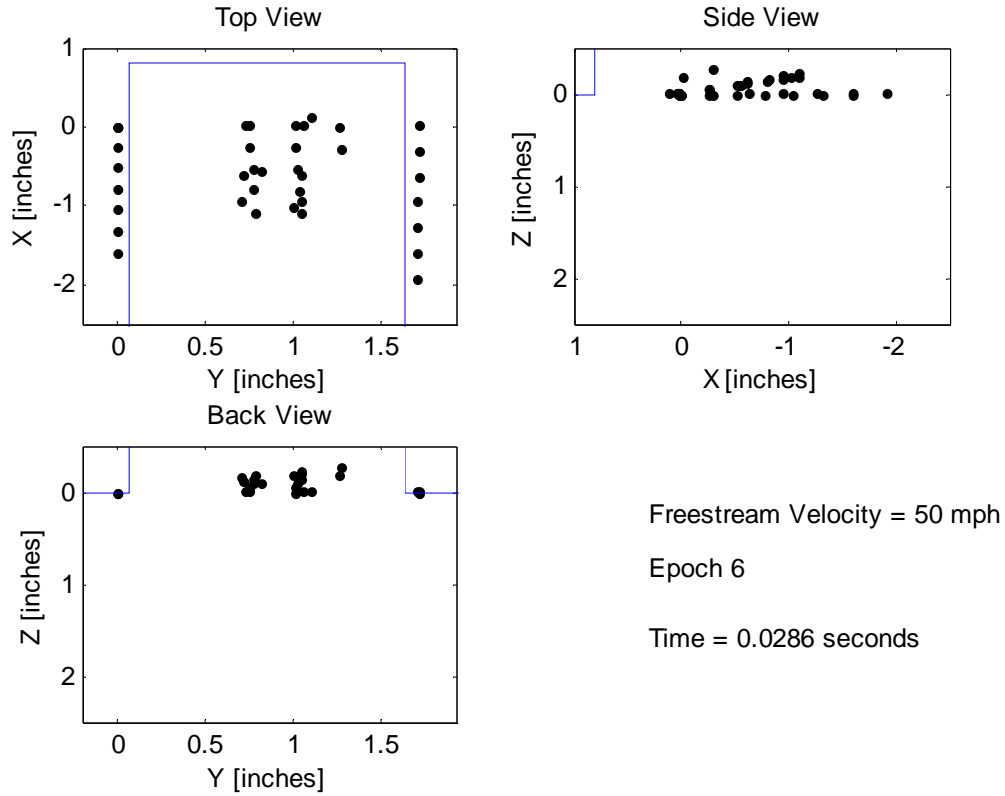
**Figure 30. Three-view of PhotoModeler® output. Epoch 21,  $V_{\infty} = 0$  mph**

Figure 30 displays the final epoch considered for the initial  $V_{\infty} = 0$  mph test. The model blocked three reference points from at least two of the cameras, resulting in fifteen usable reference points. Twenty-eight common marker points defined the model geometry. The model is out of the cavity and traveling into what would be the freestream flow. The aft view shows the model body curvature, but not the 1.0-inch diameter expected. Because some of the marker points were only visible by two cameras, PhotoModeler® could not determine their location with the same precision. As a result, the computer model had less curvature than the store model. The 0.0858-second video considered here equates to 0.384 seconds at full scale. While this is below the half second usually analyzed, the video captured the model's motion through what would have been the three phases of store release had the tunnel freestream been non-zero.



**Figure 31. Three-view of PhotoModeler® output. Epoch 1,  $V_{\infty} = 50 \text{ mph}$**

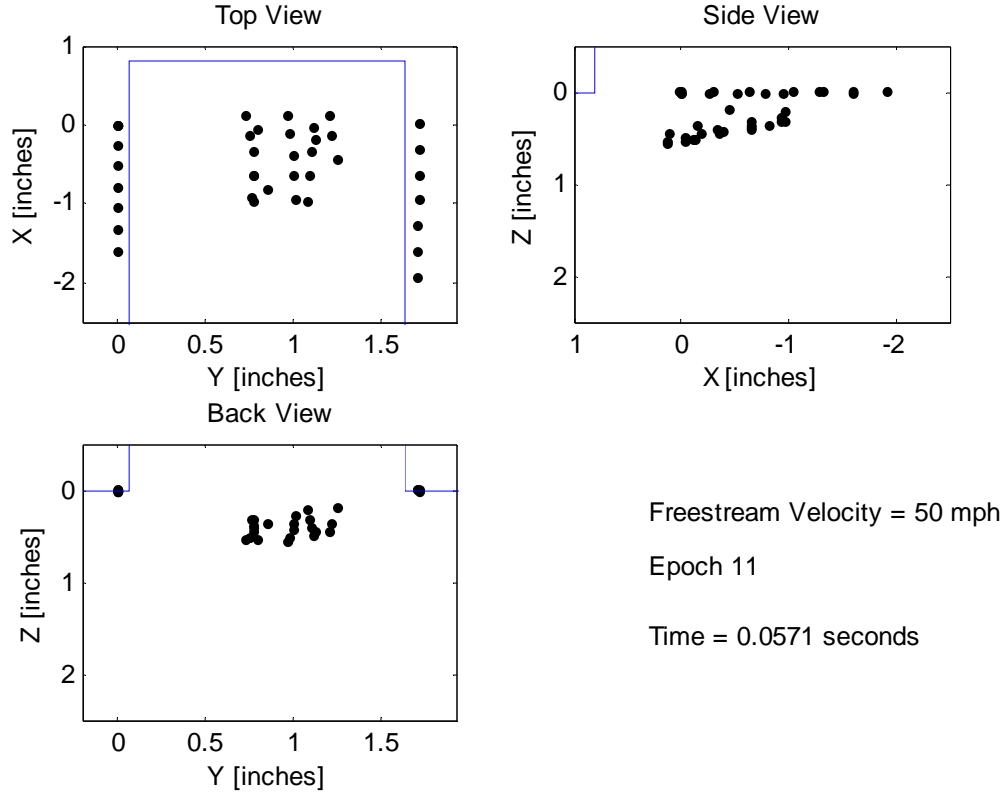
The second test occurred at freestream velocity of  $V_{\infty} = 50 \text{ mph}$ . Fourteen reference points defined the coordinate axis and scale. PhotoModeler® processed every fourth frame to create 21 epochs. Again, figures are presented using the wind axis system and the reference points are 1.715 inches apart. As seen in Figure 31, eighteen marker points defined the store model geometry inside the cavity. PhotoModeler® processed a second test at 50 mph for a repeatability study. The results are shown in Appendix B.



**Figure 32. Three-view of PhotoModeler® output. Epoch 6,  $V_{\infty} = 50 \text{ mph}$**

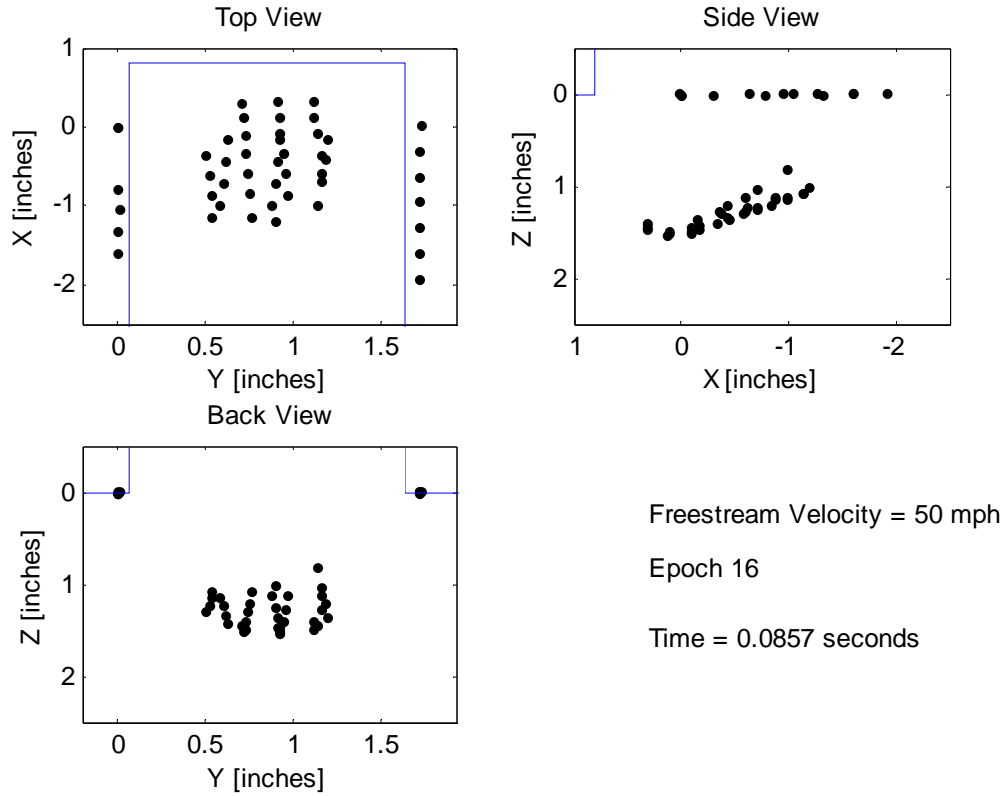
Epoch 6, seen in Figure 32, had fourteen reference points and twenty-one marker points. The model has started to fall through the cavity with a slight nose-down attitude, suggesting the release mechanism held the model aft of the center of gravity. The store model is about to cross through the shear layer. As seen in the top view, the marker points created two distinct lines running down the model body, which defined the angle of attack and store location but did not clearly define the curvature of the 1.0-inch diameter store body.





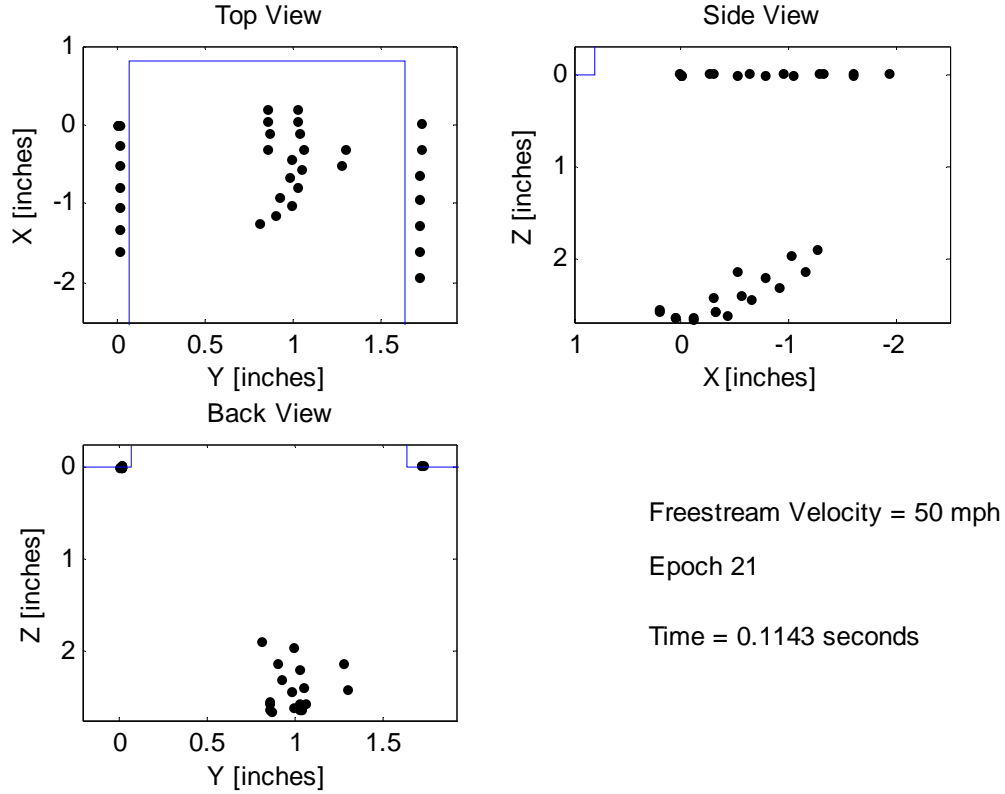
**Figure 33. Three-view of PhotoModeler® output. Epoch 11,  $V_{\infty} = 50 \text{ mph}$**

At  $t = 0.0571 \text{ sec}$ , Figure 33 depicts the second phase of store separation. There were fourteen reference points and twenty-one marker points. The model continued to nose down through the test. As the model moved relative to each laser source, the two lines of marker points seen in epoch 6 had split to become four lines, which still defined the store profile and angle of attack. However, PhotoModeler® modeled the curvature of the store body due to increased point coverage. Despite this improvement, the nose of the store model was not visible at this epoch. Tracking the nose movement was the easiest way to detect lateral translation. However, only the body of the model was reproduced in this epoch. For model movement to be detected, the scale of the movement must be on the order of the scale of the laser grid spacing. Despite a 50 mph freestream velocity, the model had not noticeably moved aft. Imagery for epochs 11-16 are included in Appendix A.



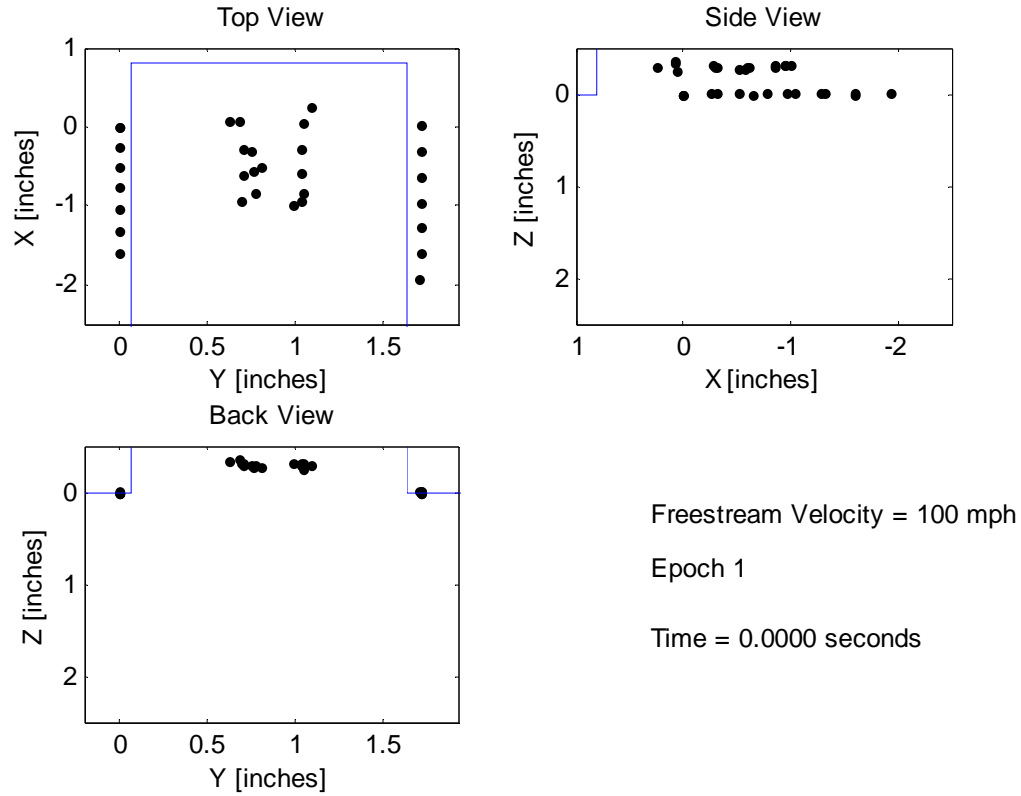
**Figure 34. Three-view of PhotoModeler® output. Epoch 16,  $V_{\infty} = 50 \text{ mph}$**

In Figure 34, the model is out of the shear layer and traveling into the freestream flow. The model had blocked reference points, leaving eleven common reference points. However, thirty-five marker points defined the model geometry. The high number of marker points yielded a higher fidelity model. As the model cleared the cavity walls, PhotoModeler® triangulated points on the spherical nose cone, making it appear the model moved forward, while closer examination revealed the model had moved aft. With the nose curvature modeled, the user could accurately track the model location and orientation in time. The side view clearly shows the orientation of the model.



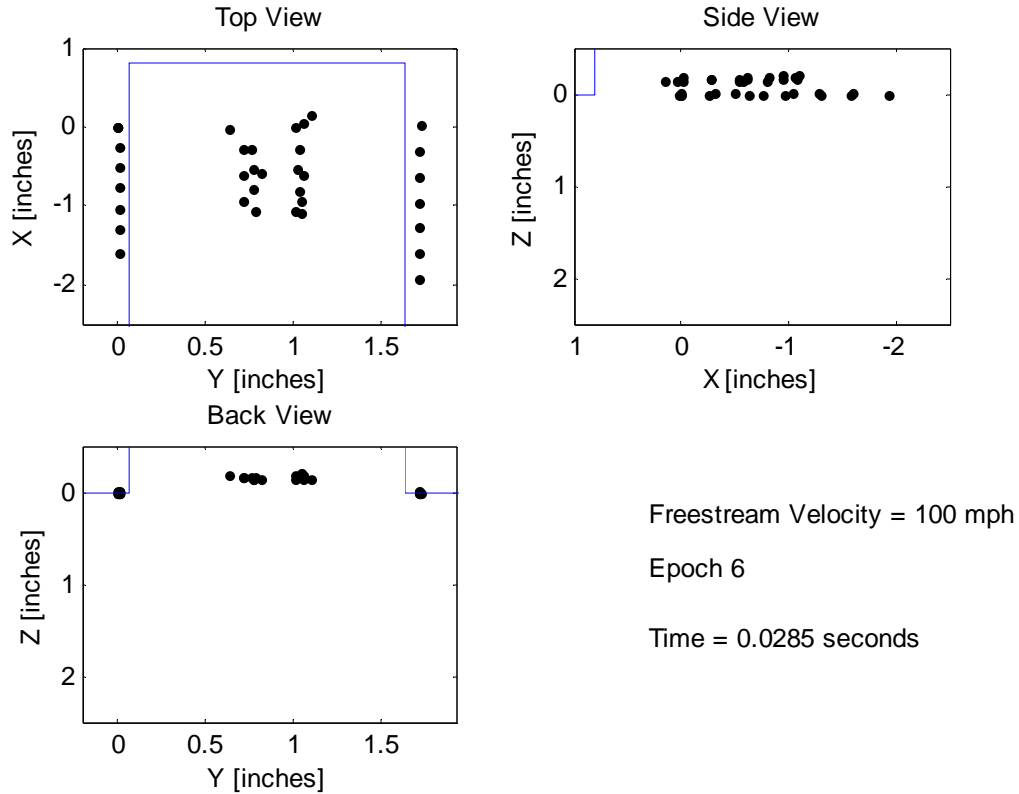
**Figure 35. Three-view of PhotoModeler® output. Epoch 21,  $V_{\infty} = 50 \text{ mph}$**

Figure 35 displays the final epoch considered for the  $V_{\infty} = 50 \text{ mph}$  test. All fourteen reference points were visible again, and eighteen marker points defined the model geometry. Additional points were visible in the raw imagery, but there were not sufficient commonality to maintain the thirty-five marker points from epoch 16. Surface imperfections could have caused poor reflections, explaining the decreased image quality. The model is out of the cavity and traveling through the tunnel freestream flow, pushing the model further downstream. The video clip represented in Figure 24 suggests that additional epochs would show the model accelerating downstream. The 0.1143-second video considered here at the wind tunnel scale equates to 0.511 seconds at full scale, exceeding the half second usually analyzed at full scale.



**Figure 36. Three-view of PhotoModeler® output. Epoch 1,  $V_{\infty} = 100 \text{ mph}$**

The third test occurred at freestream velocity of  $V_{\infty} = 100 \text{ mph}$ . Fourteen reference points defined the coordinate axis and scale. PhotoModeler® processed every fourth frame to create 21 epochs. Again, images are presented using the wind axis system and the reference points are 1.715 inches apart. As seen in Figure 36, seventeen marker points define the store model geometry inside the cavity.



**Figure 37. Three-view of PhotoModeler® output. Epoch 6,  $V_{\infty} = 100$  mph**

In Figure 37, the model has begun to fall in the cavity. Fourteen reference points and nineteen marker points defined the geometry. Similar to the  $V_{\infty} = 50$  mph test discussed above, the marker points fell largely in two lines. This was a level release, as the model had no measurable attitude. Variations in loading and releasing the store explain the slight variation in model attitude between tests. Stores were loaded visually level in the cavity before each test. During the process it was assumed the store models were made with uniform density, meaning the CG would not change location between tests. Small variations in the relationship between the store model CG and the attachment point yielded non-zero model angles of attack after release. The absence of control surfaces allowed the model to diverge and tumble uncontrolled down the tunnel. However, the cameras captured the model motion and PhotoModeler® created a 3-D model that corresponds to the actual store motion, regardless of orientation.

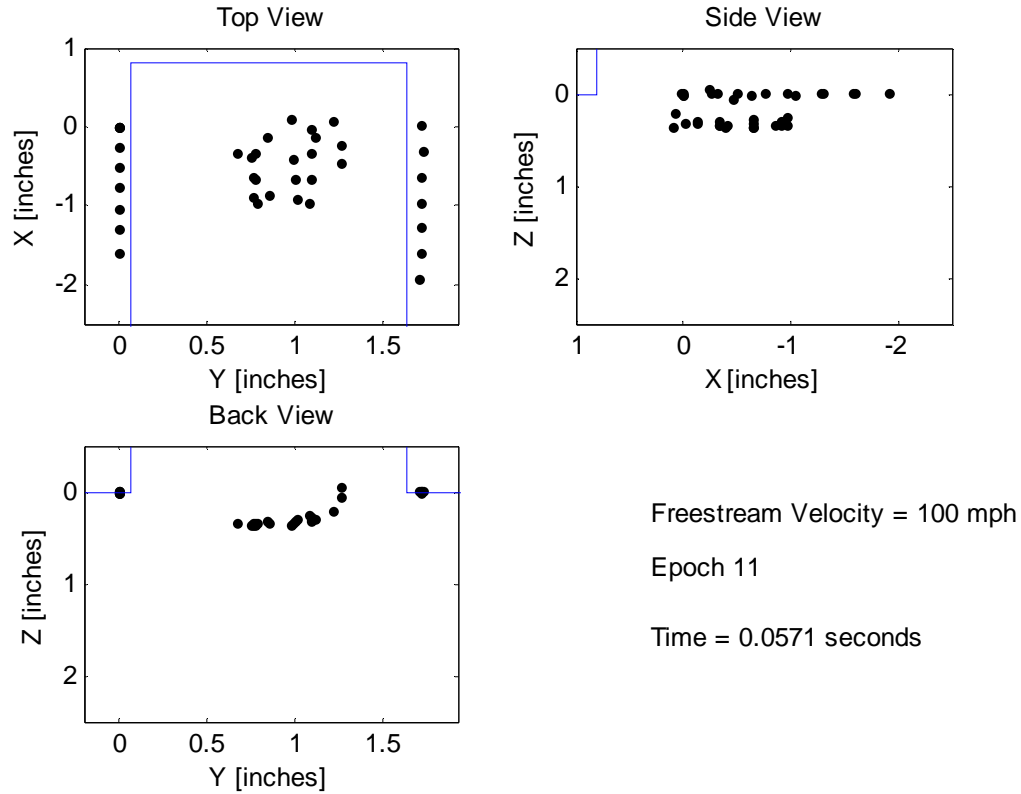


**Figure 38. Three-view of PhotoModeler® output. Epoch 11,  $V_{\infty} = 100 \text{ mph}$**

The model is in phase two of store separation in Figure 38. Fourteen reference points and twenty-one marker points defined the geometry. The laser stand vibrated because it projected into the freestream flow, which resulted in small reference and marker point movement independent of the model movement. These vibrations were small enough to yield useful data, but the model precision suffered. However, PhotoModeler® tracked model location through the test. The aft view shows the store model body curvature, which did not correspond to the 1.0-inch diameter of the store model. The ‘flat’ body curvature illustrates the effects of only having two cameras determine point location in 3-D space.

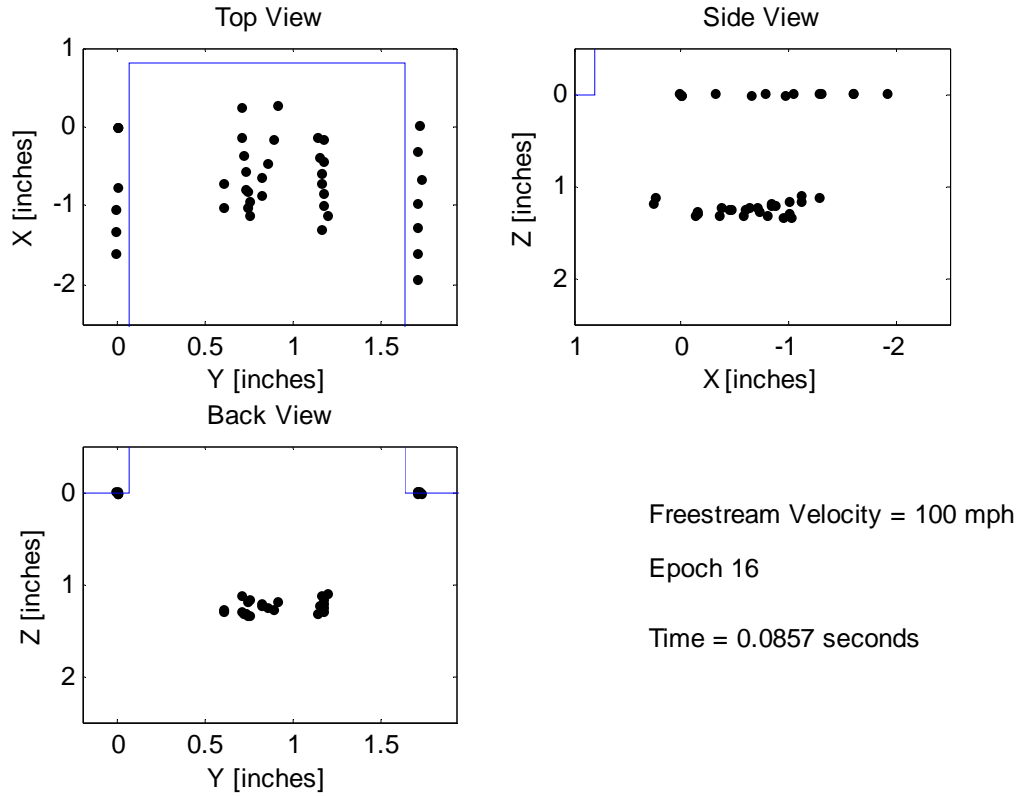


**Figure 39. Three-view of PhotoModeler® output. Epoch 16,  $V_{\infty} = 100 \text{ mph}$**

Epoch 16, seen in Figure 39, shows the model out of the shear. The model blocked three reference points from at least two of the cameras, resulting in twelve usable reference points. Twenty-six common marker points defined the model geometry. The higher freestream velocity caused aft movement as soon as the model fell through the shear layer. Despite a level release, the model showed a slight nose-down attitude. Without any control surfaces, the model should not fall perfectly orientated into the freestream flow through the test. Any instability caused by the turbulent flow in this regime would cause the model to diverge in some direction. Epoch 16 first shows this angular motion.

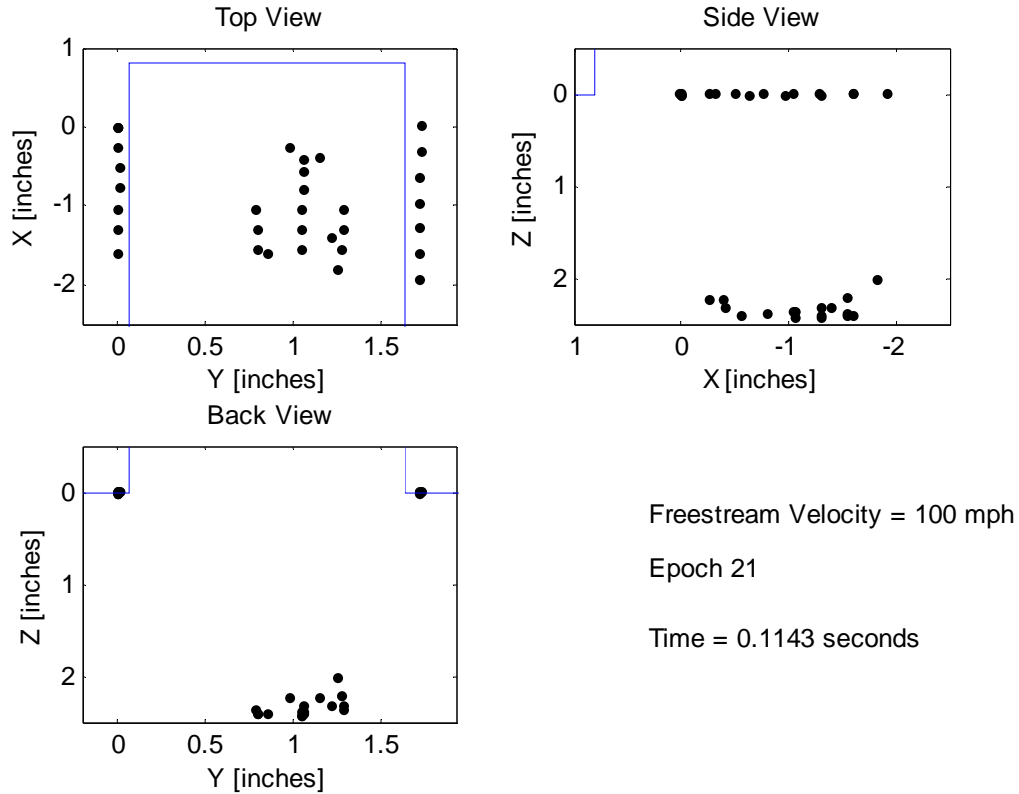


**Figure 40. Three-view of PhotoModeler® output. Epoch 21,  $V_{\infty} = 100$  mph**

The model has fallen sufficiently in Figure 40 to restore all fourteen original reference points. Seventeen marker points define the model geometry. At this point, the store has traveled through the shear layer into the freestream flow. As the model accelerated downstream, the nose-down attitude continued to increase. The 0.1143-second video considered here equates to 0.511 seconds at full scale, exceeding the half second usually analyzed in full-scale tests.

The selected epochs above show model movement and the software's ability to create moving three-dimensional models. Even with reference some points blocked, the software accurately triangulated each point's location because the user defined the axis and scale with all points visible. The  $V_{\infty} = 0$  mph calibration test confirmed the process for model fabrication and image processing. The  $V_{\infty} = 50$  mph test released the store model with a slight nose-down attitude, which increased through the test before tumbling uncontrolled down the wind tunnel. The  $V_{\infty} = 100$  mph test released the store model level, but flow instabilities caused the model to



nose-down late in the test. In all, the tests presented here all showed the instability of the store model and the ability to create quality 3-D moving models.

## **V. Conclusions and Recommendations**

A series of store separation experiments, performed using models composed of dry ice, demonstrated that model location could be quantified using high speed cameras and dot-projection photogrammetry. Wind tunnel fan visual inspection showed that the store model used in testing did not damage the blades or any other tunnel components. The process for model fabrication produced enough quality models for testing. However, improvements in model success rate are sought because one out of every three attempts was successful. While vents in the mold improved model quality, they also decreased the probability of an acceptable model formation.

High-speed photogrammetry enables tracking of moving models and leads to a 3-D representation of the model shape and trajectory. Three small 5mW lasers fitted with pattern generating optics and mounted on the wind tunnel sting illuminated the store and cavity with marker points and reference points, respectively. Each model, with a 1.0-inch diameter and 1.8-inch length, was large enough to accommodate up to 35 marker points on its surface. A high point density leads to an accurate portrayal of model shape. However, such a high point density complicates processing because PhotoModeler® confuses point location when points are dense and moving rapidly. Manual input was required to ensure accuracy throughout the tracking process.

Wind tunnel testing utilized freestream velocities of 50 and 100 mph, while a control test occurred at zero velocity. The model approximately corresponded to a 5% scale of a Mk-81 with 9-inch diameter, 74-inch length, and 262 lb. mass. Assuming a release at 10,000 ft. altitude, the two tunnel velocities used in the tests correspond to flight speeds of 224 mph and 447 mph with Froude scaling applied.

The use of nonintrusive free-drop measurements guarantees the behavior of the store is representative because no modifications were needed to add measurement equipment. Visual

tracking techniques combined with modern computing capabilities create a powerful tool able to provide high-quality moving models of store separation.

Accurately scaling models and using materials that will not harm expensive wind tunnel components opens the door to store drop tests in a wind tunnel. By forming store models of inexpensive and environmentally friendly dry ice, this proof-of-concept may enable more rigorous testing to complement computation codes, such as BEGGAR, captive trajectory tests and flight testing.

### **Recommendations for Future Work**

The dry ice fabrication process used was originally successful about 60% of the time. After drilling small vent holes in the side of the mold, successful models were of higher quality but were less common. Further experimentation with filters, technique, and hardware might increase the chances of producing quality models. Purchasing a commercial system might aid in this process.

This model had the basic shape of a simple bullet, but most missiles and bombs have geometries that are more complex. While the precise motion of the store was not a key concern for developing this modeling and tracking technique, it will provide direct application to future projects if testing continues with model geometries that are more representative of current munitions. A better fabrication process, as described above, would also aid in producing models that are more complex.

While modeling the release of a store from a cavity at Mach 0.8 is useful, this research has been ongoing for decades. Move future experiments into a high-speed or supersonic wind tunnel. This will better represent current research objectives.

Again, because this research was more concerned with modeling and tracking than specific store motion, the scaling laws did not need to be followed exactly. However, if addressing the above problems, there is every reason to match the scaling laws as closely as

possible. In wind tunnels where the user has significant control over test conditions, limiting model density is of less importance.

The experimental setup described above worked adequately for this project, but needs to improve for future developments. Installing a pneumatic solenoid to control the release mechanism would simplify the test procedures as well as improve repeatability. In addition, rearranging the setup would allow a single user to control the cameras and wind tunnel from the same computer terminals. If done properly, a single user could control the entire experiment. These changes would make results more repeatable because there would be no direct human input other than installing the model.

Due to the high point density, crossing point paths, and constant adding and deleting of points, the PhotoModeler® PMV module was unable to accurately and reliably tracking the points. The PMV module did an adequate job during the initial movement of the model immediately after store release, but once the model began to accelerate through the shear layer and into the aircraft model boundary layer the points moved too far between epochs. The software algorithms could not properly identify how points correlated between epochs. A different software package might better handle these issues. Another solution would be to use a single light source, which would eliminate the case of laser points crossing each other.

## Appendix A: Imagery for Epochs 11-16, $V_{\infty} = 50 \text{ mph}$

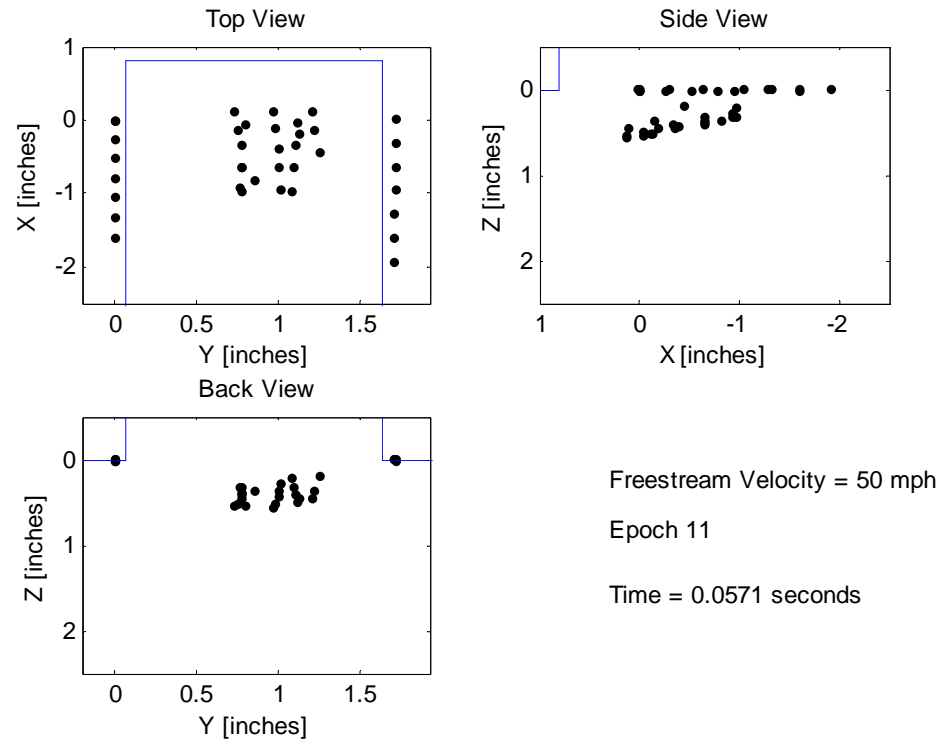


**Figure 41. Three-view of PhotoModeler® output. Epoch 11,  $V_{\infty} = 50 \text{ mph}$**

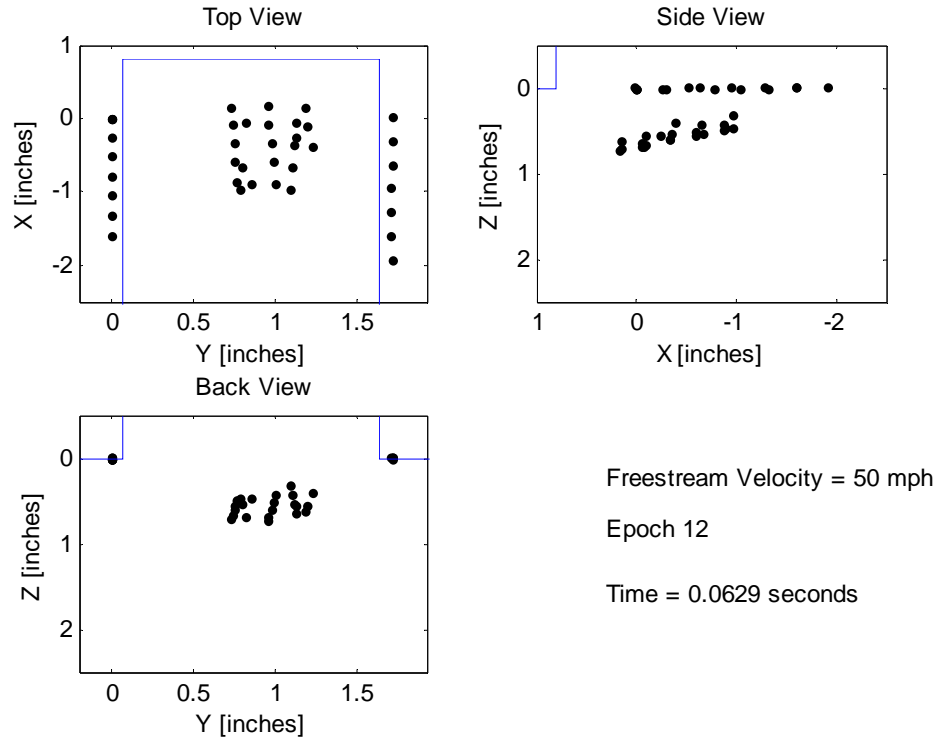


**Figure 42. Three-view of PhotoModeler® output. Epoch 12,  $V_{\infty} = 50 \text{ mph}$**

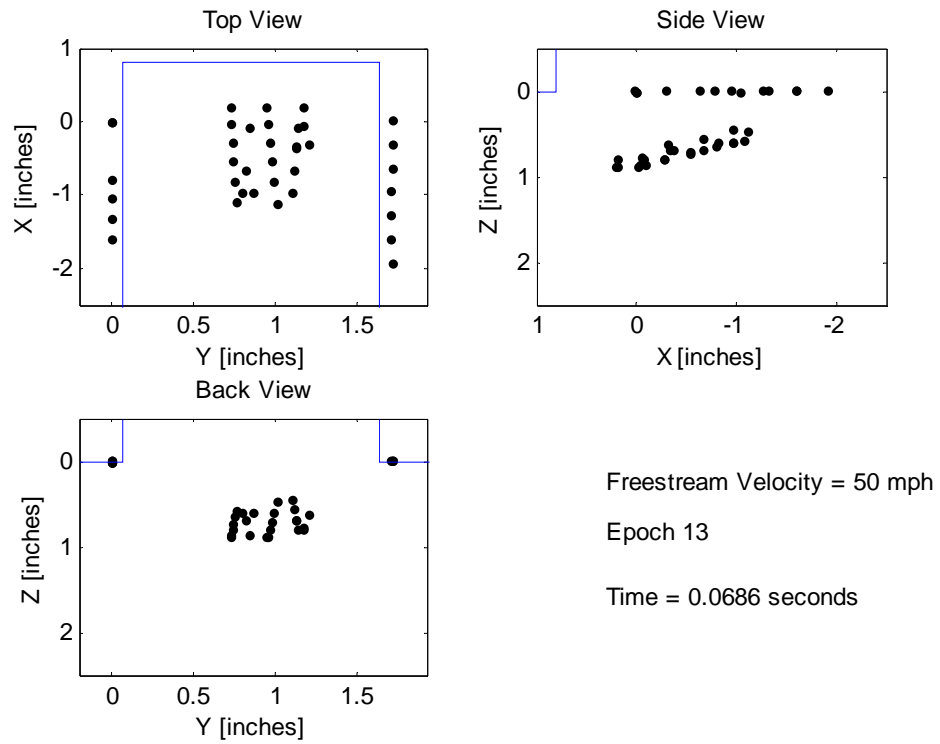


**Figure 43. Three-view of PhotoModeler® output. Epoch 13,  $V_{\infty} = 50 \text{ mph}$**

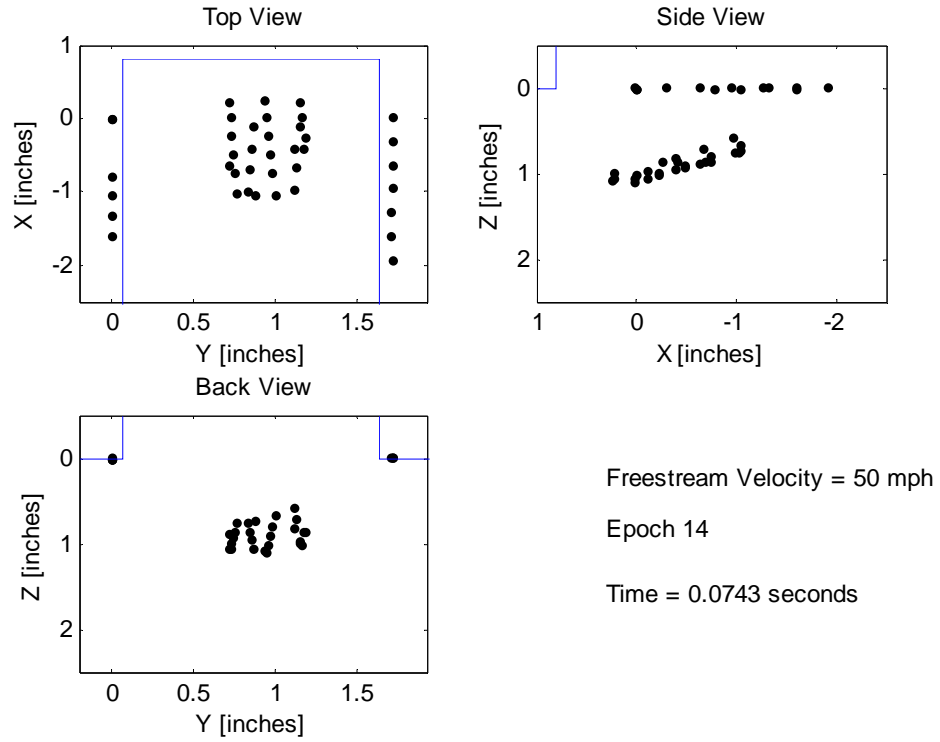


**Figure 44. Three-view of PhotoModeler® output. Epoch 14,  $V_{\infty} = 50 \text{ mph}$**

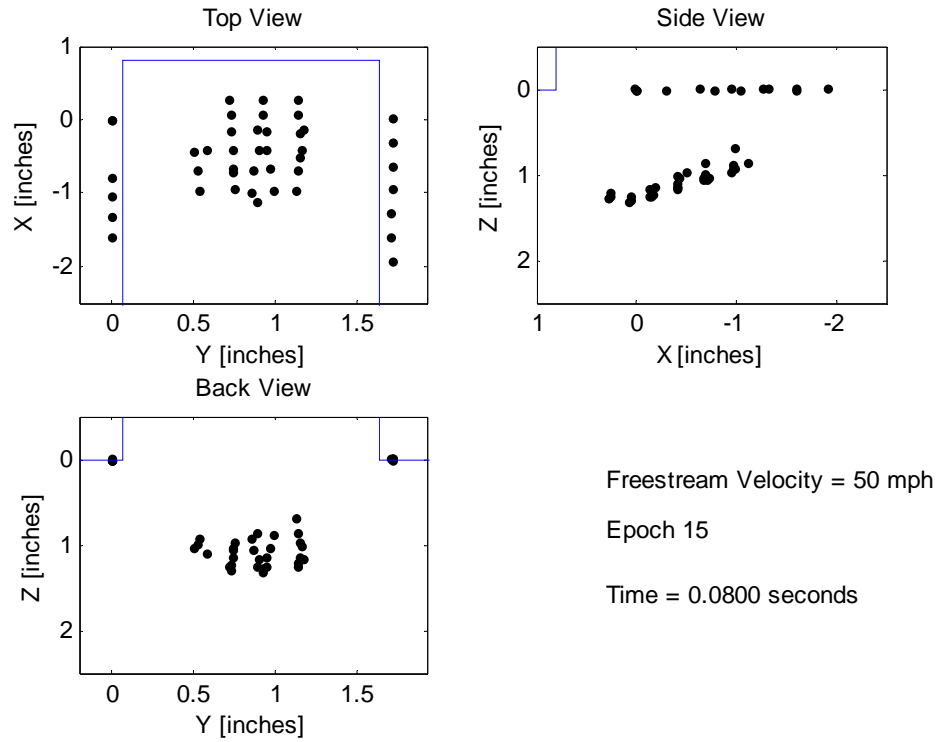


**Figure 45. Three-view of PhotoModeler® output. Epoch 15,  $V_{\infty} = 50 \text{ mph}$**

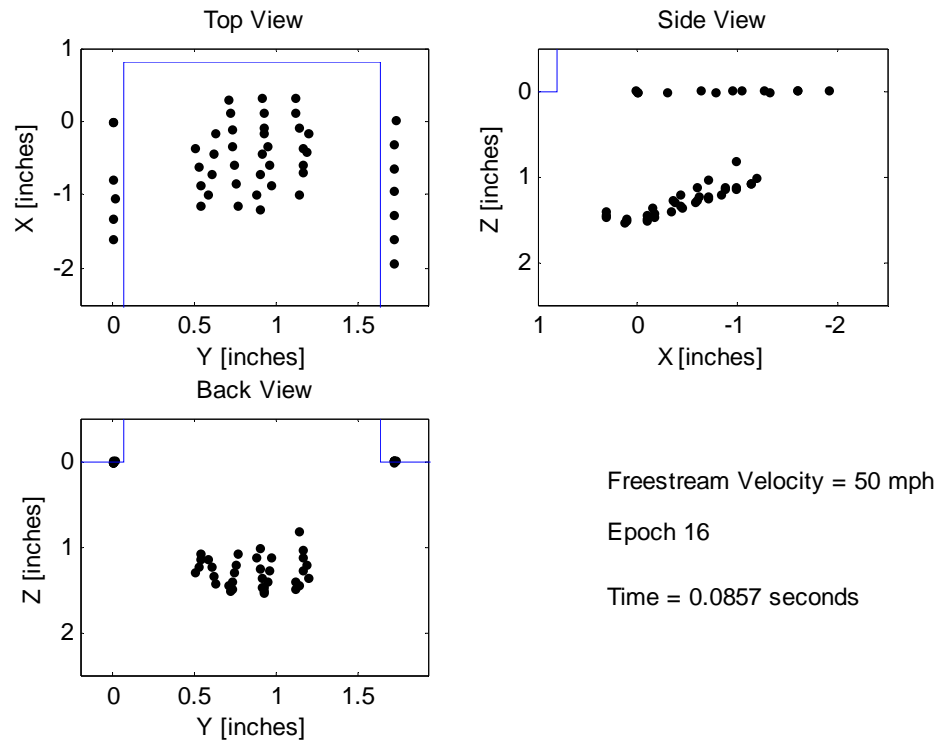


**Figure 46. Three-view of PhotoModeler® output. Epoch 16,  $V_{\infty} = 50 \text{ mph}$**



## Appendix B: Repeatability Check

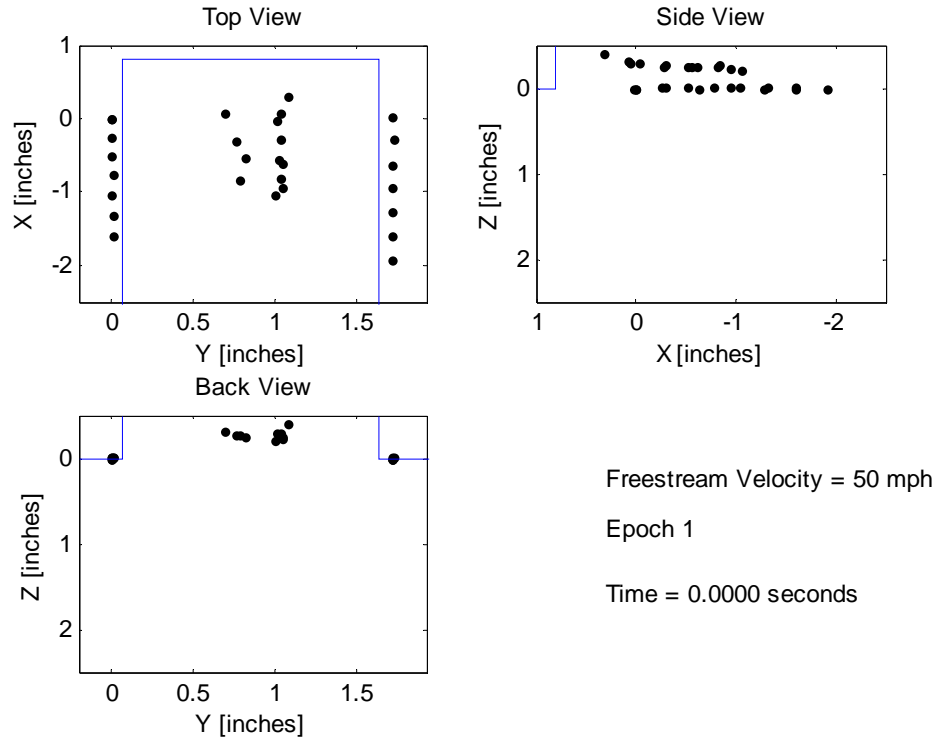


**Figure 47. Three-view of PhotoModeler® output. Epoch 1,  $V_{\infty} = 50 \text{ mph}$**

Analyzing a second 50 mph run shows similar results as discussed before. This separation maintained a nose-up attitude after release. PhotoModeler® processed eighteen epochs, creating a computer model of the initial 0.0971 seconds of store release.

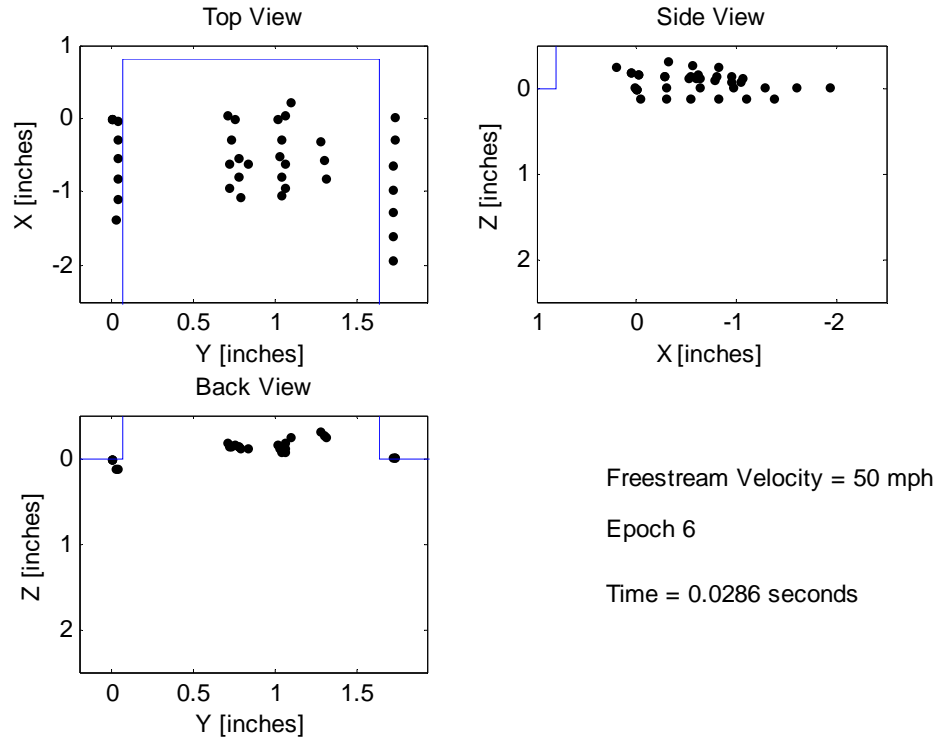


**Figure 48. Three-view of PhotoModeler® output. Epoch 6,  $V_{\infty} = 50$  mph**

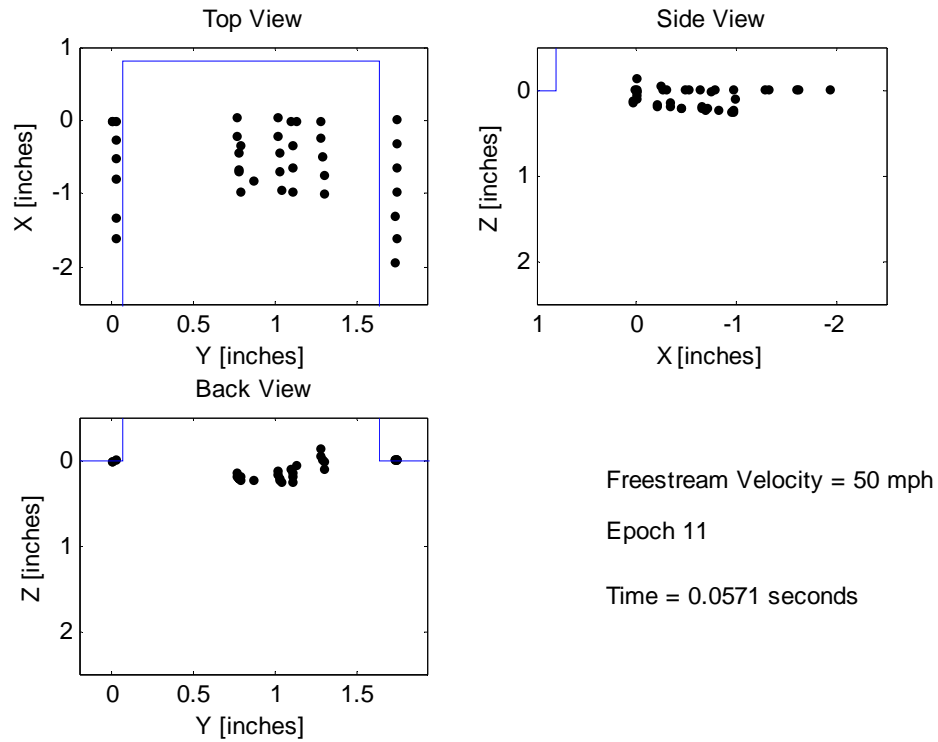


**Figure 49. Three-view of PhotoModeler® output. Epoch 11,  $V_{\infty} = 50$  mph**

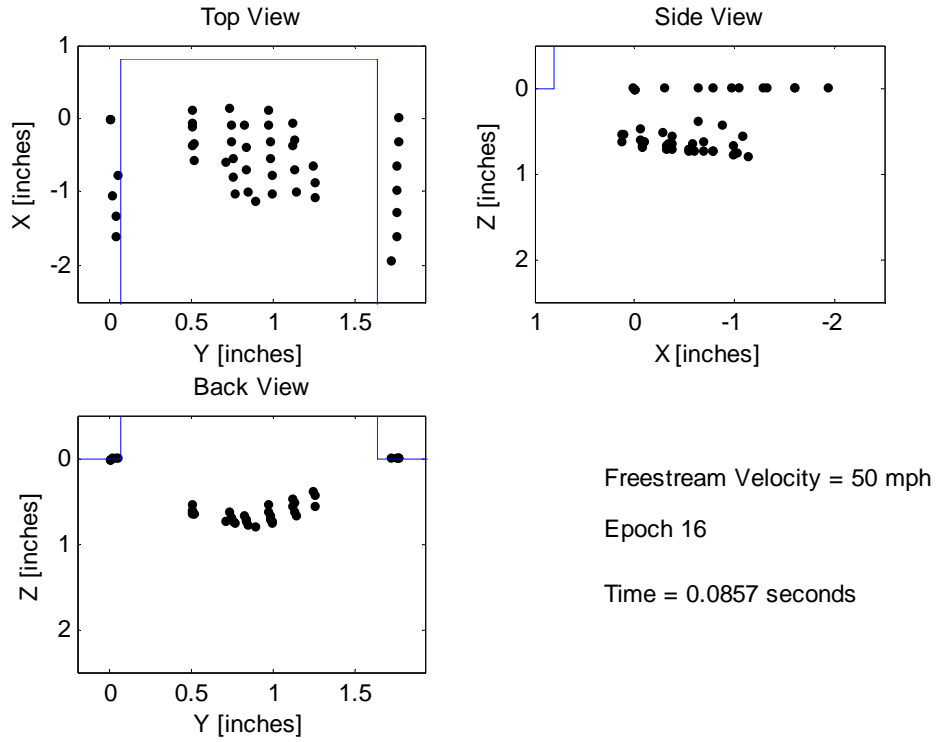


**Figure 50. Three-view of PhotoModeler® output. Epoch 16,  $V_{\infty} = 50$  mph**

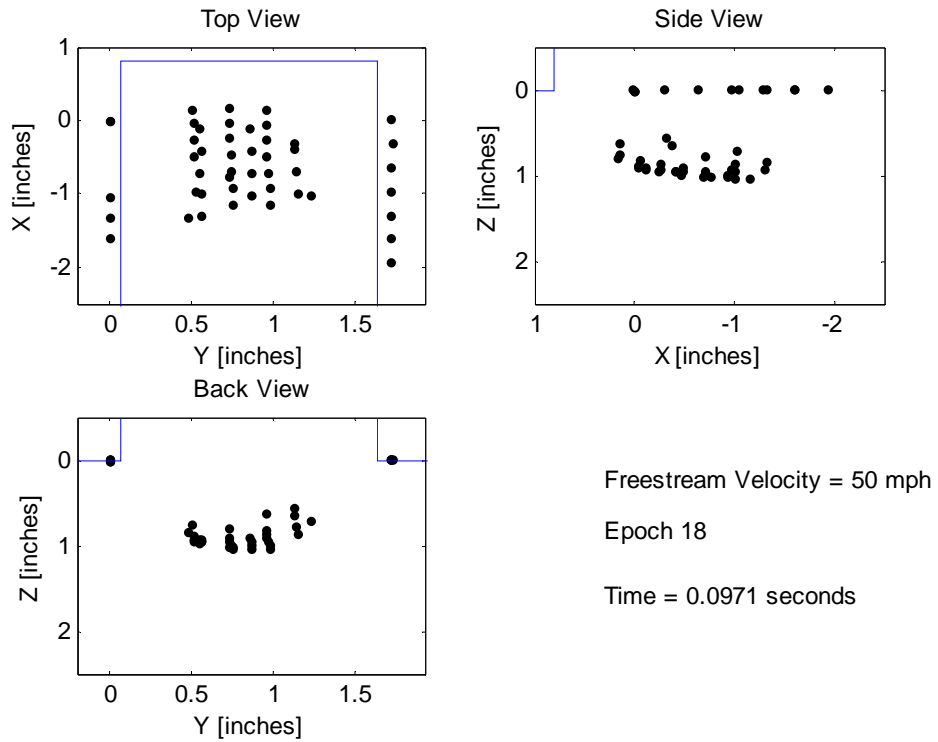


**Figure 51. Three-view of PhotoModeler® output. Epoch 18,  $V_{\infty} = 50$  mph**

## Bibliography

- [1] Rudy A. Johnson, Michael J. Stanek, and James E. Grove, "Store Separation Trajectory Deviations Due to Unsteady Weapons Bay Aerodynamics," Reno, Nevada, *AIAA 2008-188*, January 7-10, 2008.
- [2] Nathan E. Murray, Bernard J. Jansen, Lichuan Gui, John M. Seiner, and Roger Birkbeck, "Measurements of Store Separation Dynamics," 47th AIAA Aerospace Sciences Meeting including The New Horizons Forum and Aerospace, Orlando, FL, Florida, *AIAA 2009-105*, January 5-9, 2009.
- [3] V. I. Shalaev, A. V. Fedorov, and N. D. Malmuth, "Dynamics of Slender Bodies Separating from Rectangular Cavities," 31st AIAA Fluid Dynamics Conference and Exhibit, Anaheim, California, *AIAA 2001-2996*, June 11-14, 2002.
- [4] John C. Marshall, "Analytical Evaluation of the Limitations of the Various Scaling Laws for Freedrop Store Separation Testing,".
- [5] Magdi Rizk, Steven Ellison, and Nathan C. Prewitt, "Beggar - A Store Separation Predictive Tool," 32nd AIAA Fluid Dynamics Conference and Exhibit, St Louis, Missouri, *AIAA 2002-3190*, June 24-26, 2002.
- [6] Jacob A. Freeman and Bruce A. Jolly, "Applied Computational Fluid Dynamics in Support of Aircraft/Store Compatibility and Weapons Integration - 2004 Edition," 44th AIAA Aerospace Sciences Meeting and Exhibit, Reno, NV, *AIAA 2006-456*, 2004.
- [7] A. Cenko et al., "IHAAA Applications to Reducing Store Separation Flight Testing," 2007 U.S. Air Force TandE Days, Destin, Florida, *AIAA 2007-1653*, February 13-15, 2007.
- [8] Scott T. Bjorge, Mark F. Reeder, C. Subramanian, Jim Crafton, and Sergey Fonov, "Flow Around an Object from a Cavity into a Supersonic Freestream," *AIAA Journal*, vol. 43, no. 7, pp. 1465-1475, July 2005.
- [9] David W. Callaway, Mark F. Reeder, Robert B. Greendyke, and Ryan Gosse, "Photogrammetric Measurement of Recession Rates of Low Temperature Ablators in Supersonic Flow," 48th AIAA Aerospace Sciences Meeting Including the New Horizons Forum and Aerospace Exposition, Orlando, Florida, *AIAA 2010-1216*, January 4-7, 2010.
- [10] David L Kohlman and Richard W Richardson, "Experiments on the Use of Dry Ice Ablating Wind-Tunnel Models," *Journal of Spacecraft and Rockets*, vol. 6, no. 9, Sept 1969.
- [11] (2011) GlobalSecurity.org. [Online].  
<http://www.globalsecurity.org/military/systems/munitions/mk81-specs.htm>

- [12] Reeder, M., Crafton, J., Estevadeordal, J., DeLapp, C.J., McNiel, C., Peltier, D., & Reynolds, T., "Clean Seeding for Flow Visualization and Velocimetry Measurements", *Experiments in Fluids*, vol. 48, no. 5, 889-900, May 2010.
- [13] A. M. DeLuca, M. F. Reeder, J. Freeman, and Michael V. Ol, "Flexible- and Rigid-Wing Micro Air Vehicle: Lift and Drag Comparison," *Journal of Aircraft*, vol. 43, no. 2, pp. 572-575, March 2006.
- [14] EoS Systems Inc., *PhotoModeler 6 User Guide.*, 2007.
- [15] K. S. Keen, C. H. Morgret, and R. L. Arterbury, "An Analytical Investigation of Accuracy Requirements for Onboard Instrumentation and Film Data for Dynamically Scaled Wind Tunnel Drop Models," Sverdrup Technology, Inc., Final Report AEDC-TR-96-7, 1997.
- [16] A. W. Cary and L. P. Wesley, "Airframe Integration of Modern Stores (AIMS), Delivery Order 0031: Phase II and III Analytical Predictions and Validations," Air Force Research Lab, Dayton, OH, AFRL-VA-WP-TR-2006-3079, January 2006.
- [17] Ronald Deslandes and Stefan Donauer, "Scaled-Drop-Tests: WYSIWYG or not?," EADS-Defence and Security, Orlando, FL, *AIAA 2010-681*, 2010.
- [18] Stephen R. Perillo and Donald Atkins, "Challenges and Emerging Trends in Store Separation Engineering - an Air Force SEEK EAGLE Office Perspective," 47th AIAA Aerospace Sciences Meeting including The New Horizons Forum and Aerospace, Orlando, Florida, *AIAA 2009-101*, January 5-9, 2009.
- [19] Robert L. Spinetti and Bruce A. Jolly, "Time-Accurate Numerical Simulation of GBU-38s Separating from the B-1B Aircraft with Various Ejector Forces, Store Properties, and Load-out Configurations - IHAAA Store Separation Cavity (SSC) Project," 46th AIAA Aerospace Sciences Meeting and Exhibit, Reno, Nevada, *AIAA 2008-187*, January 7-10, 2008.
- [20] Srinivasan Arunajatesan, Christopher Chartrand, and Roger Birkbeck, "Analysis of Unsteady Bay Shear Layer Effects on Store Separation Characteristics," 47th AIAA Aerospace Sciences Meeting including The New Horizons Forum and Aerospace, Orlando, Florida, *AIAA 2009-546*, January 5-8, 2009.
- [21] K. Scott Keen, Charles H. Morgret, T. Frank Langham, and William B. Baker, "Trajectory Simulations Should Match Flight Tests and Other Lessons Learned in 30 Years of Store-Separation Analysis," 47th AIAA Aerospace Sciences Meeting including The New Horizons Forum and Aerospace, Orlando, Florida, *AIAA 2009-99*, January 5-8, 2009.
- [22] A. Cenko, "Lessons Learned in 30 years of Store Separation Testing," 47th AIAA Aerospace Sciences Meeting including The New Horizons Forum and Aerospace, Orlando, Florida, *AIAA 2009-98*, January 5-8, 2009.

## **Vita**

Lieutenant Michael Paul grew up in Stow, Ohio before graduating from Stow-Monroe Falls High School in 2005. He attended the United States Air Force Academy and received his Bachelors of Science in Aeronautical Engineering and his commission into the United States Air Force on 27 May 2009. Upon commissioning, he attended AFIT to continue his studies of Aeronautical Engineering. Michael will continue his career at Kirtland AFB, NM where he will work in Det 12, Air Force Research Laboratories.

<b>REPORT DOCUMENTATION PAGE</b>			Form Approved OMB No. 0704-0188	
The public reporting burden for this collection of information is estimated to average 1 hour per response, including the time for reviewing instructions, searching existing data sources, gathering and maintaining the data needed, and completing and reviewing the collection of information. Send comments regarding this burden estimate or any other aspect of this collection of information, including suggestions for reducing this burden to Department of Defense, Washington Headquarters Services, Directorate for Information Operations and Reports (0704-0188), 1215 Jefferson Davis Highway, Suite 1204, Arlington, VA 22202-4302. Respondents should be aware that notwithstanding any other provision of law, no person shall be subject to any penalty for failing to comply with a collection of information if it does not display a currently valid OMB control number. PLEASE DO NOT RETURN YOUR FORM TO THE ABOVE ADDRESS.				
1. REPORT DATE (DD-MM-YYYY) 24-03-2011		2. REPORT TYPE Master's Thesis		3. DATES COVERED (From — To) 1 Sept 09 – 24 March 11
4. TITLE AND SUBTITLE Experimental Measurements of Store Separation Using Dry Ice Models in A Subsonic Flow			5a. CONTRACT NUMBER	
			5b. GRANT NUMBER	
			5c. PROGRAM ELEMENT NUMBER	
6. AUTHOR(S) Michael C Paul, 2d Lt, USAF			5d. PROJECT NUMBER	
			5e. TASK NUMBER	
			5f. WORK UNIT NUMBER	
7. PERFORMING ORGANIZATION NAME(S) AND ADDRESS(ES) Air Force Institute of Technology Graduate School of Engineering and Management (AFIT/ENY) 2950 Hobson Way WPAFB OH 45433-7765			8. PERFORMING ORGANIZATION REPORT NUMBER AFIT/GAE/ENY/11-M23	
9. SPONSORING / MONITORING AGENCY NAME(S) AND ADDRESS(ES) AFRL/RBAI 2145 5TH ST Wright Patterson AFB, OH 45433 POC: Mr. Rudy Johnson, 937-785-3037 Rudy.Johnson@wpafb.af.mil			10. SPONSOR/MONITOR'S ACRONYM(S) AFRL/RBAI	
			11. SPONSOR/MONITOR'S REPORT NUMBER(S)	
12. DISTRIBUTION / AVAILABILITY STATEMENT APPROVED FOR PUBLIC RELEASE; DISTRIBUTION UNLIMITED				
13. SUPPLEMENTARY NOTES This material is declared a work of the US government and is not subject to copyright protection in the United States.				
14. ABSTRACT Testing free-drop store separation from a cavity in wind tunnels proves a difficult task because the models are typically destroyed during the test. Furthermore, there is potential for damage to wind tunnel components. Prior work has shown that small dry ice models released within the test section do not cause damage to the AFIT pressure-vacuum wind tunnel components or vacuum chamber. Rather, the dry ice models break apart and sublime harmlessly into gaseous carbon dioxide. Therefore, this study was undertaken to determine whether dry ice models might prove useful in free-drop store separation testing. A generic aircraft cavity was constructed for testing in the AFIT low speed wind tunnel. Stores were formed by directly injecting pressurized liquid carbon dioxide into a mold. The store geometry used is a circular cylinder with spherical nosecone, with 1.0-inch diameter by 1.8 inches in length. Three 5mW lasers fitted with pattern generating optics were mounted on the wind tunnel sting to illuminate the store and cavity. Three high-speed cameras recorded each test at 700 frames per second and the models were tracked using laser dot projection photogrammetry. Experiments were conducted at nominal freestream velocities of 0, 50, and 100 mph.				
15. SUBJECT TERMS Store separation, dry ice models, photogrammetry				
16. SECURITY CLASSIFICATION OF:			17. LIMITATION OF ABSTRACT  UU	18. NUMBER OF PAGES  87
a. REPORT  U	b. ABSTRACT  U	c. THIS PAGE  U		
			19a. NAME OF RESPONSIBLE PERSON Dr. Mark F. Reeder	
			19b. TELEPHONE NUMBER (Include Area Code) (937) 785-3636, x4530 Email: Mark.Reeder@afit.edu	

Standard Form 298 (Rev. 8-98)  
Prescribed by ANSI Std. Z39.18